Supplementary Information for: A Decadal-Scale Perspective on PM_{10} Composition and its Variability Drivers at the Alpine High-Altitude Research Station Jungfraujoch

Julian Weng[1], Yufang Hao[1], Benjamin T. Brem[1], Tianqu Cui[1], Peeyush Khare[1,7], Lubna Dada[1], Kaspar R. Daellenbach[1], Sophie Darfeuil[2], Gaëlle Uzu[2], Jean-Luc Jaffrezo[2], Martin Steinbacher[3], Stefan Reimann[3], Thaleia Gkraikou[4], Konstantina Oikonomou[4], Jean Sciare[4], Martine Collaud Coen[5], Claudia Mohr[1,6], Andre S. H. Prévôt[1], Martin Gysel-Beer[1], Imad El Haddad[1], and Patrik Winiger[1]

[1]PSI Center for Energy and Environmental Sciences, 5232 Villigen PSI, Switzerland
[2]Université Grenoble Alpes, CNRS, INRAE, IRD, G-INP, IGE, 38000 Grenoble, France
[3]Swiss Federal Laboratories for Materials Science and Technology, Empa, 8600 Dübendorf, Switzerland
[4]Climate and Atmosphere Research Center, The Cyprus Institute, Nicosia, 2121, Cyprus
[5]Federal Office of Meteorology and Climatology, MeteoSwiss, 1530 Payerne, Switzerland
[6]Department of Environmental Systems Science, ETH Zurich, 8092 Zürich, Switzerland
[7]Now at: Institute of Climate and Energy Systems (ICE–3): Troposphere, Forschungszentrum Jülich, 52428 Jülich, Germany

Correspondence: Patrik Winiger (patrik.winiger@psi.ch)

Contents

S1 Sample selection strategy and filtering of Saharan dust influenced composite samples

S1.1 Sample selection strategy for 11-year composite filter samples

Daily PM_{10} filters were pooled into composites of four at an interval of four days for chemical analysis (Figure S1). This sampling strategy was selected as an optimal trade-off between establishing a long-term analyzed time series, maximizing sample representativeness, and maintaining a practicable level of laboratory analytical workload.

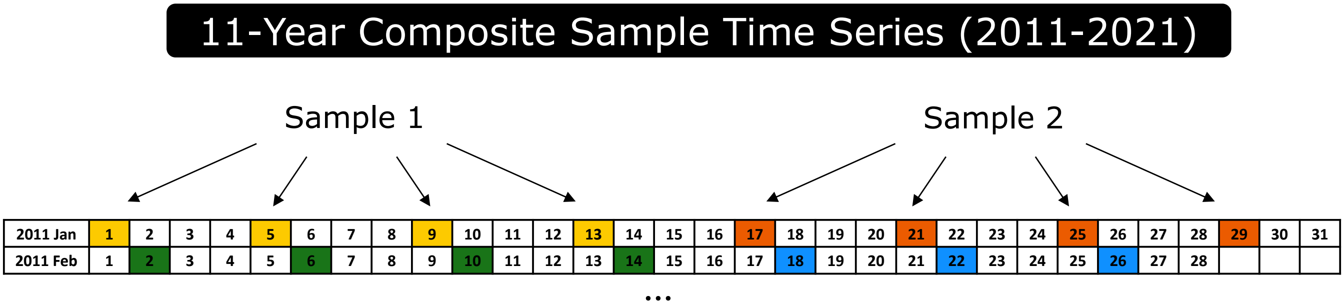

Figure S1. Schematic of filter sample selection and pooling strategy employed for the 11-year composite samples. Filters pooled for each set of consecutive samples are denoted by a distinct color. For plotting of composite data, always the earliest filter sampling date is used (for example Jan 1st 2011 for *Sample 1* and Jan 17th 2011 for *Sample 2*).

To assess how well reduced sampling frequencies represent the full daily-resolution time series, the effect of selecting every second, third or fourth observation from the full dataset was evaluated and its ability to reproduce both short- and medium-term variability was examined. For this evaluation, daily sulfate mass concentrations, measured by Ion Chromatography (IC), and gravimetrical PM_{10} were utilized (both from PM_{10} filters, measured as part of the *Swiss National Air Pollution Monitoring Network* (Hueglin et al., 2024)). Because sampling every k days can begin on any of the n possible phase offsets, we evaluated four offsets corresponding to sampling starting on day 1, 2, 3, or 4 of the full record. For each offset, every k-th value was extracted to form a subsample, and each subsample value was compared with the corresponding k-day block mean computed directly from daily concentrations. Representativeness was then quantified using the integral of the spectral power (Venables and Ripley, 2002) between the subsample strategy and the true block means. An optimal trade-off was found for composites of four samples at an interval of four days.

To confirm this selection further, we quantified the bias, root-mean-square error (RMSE), correlation, distributional differences, and the ratio of standard deviations between our strategy and the true block means. To evaluate potential aliasing introduced by the reduced sampling interval, we computed the smoothed spectral density of the full daily series and quantified the proportion of total spectral power lying below the Nyquist frequency ($= 1/(2 \times dt)$, where $dt = 4days$ (Infante et al., 2021)) associated with sample selection every 4 days (0.125 cycles per day). In a second step, we evaluated the performance of daily sample values mimicking composite sample values. Groups of four consecutive subsample points (spanning 16 days) were averaged to produce composite values, which were compared against the corresponding 16-day block means from the full daily record of sulfate and PM_{10} concentrations (cf. Figure S2 for sulfate). The same performance metrics were then applied to quantify how well the composite measurements reflect the true aggregated signal.

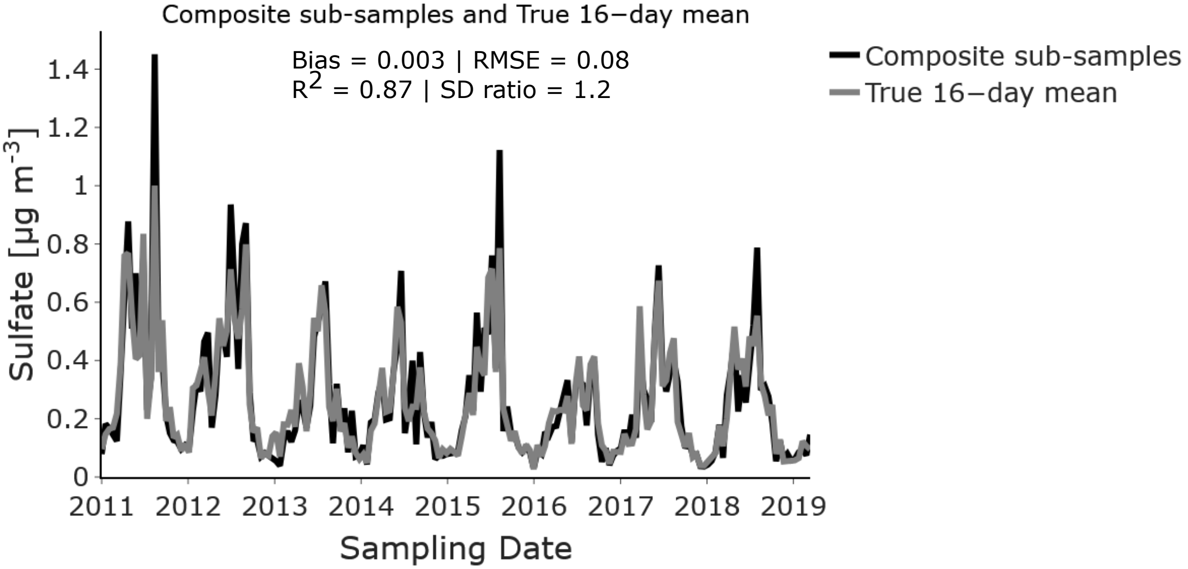

Figure S2. Sulfate mass concentration time series (2011 to February 2019) for 16-day composites sub-samples and true 16-day mean values of the same periods. The bias, RMSE, R^2 and ratio of standard deviations are provided.

S1.2 Detection of Saharan dust events at the JFJ by aerosol optical properties

Collaud Coen et al. (2004) introduced a binary method for detection of Saharan dust plumes at the JFJ, based on aerosol optical characteristics. It utilizes the change of the wavelength dependence (i.e. the Ångström exponent) of the single scattering albedo (SSA) during dust events. The larger particle size and different chemical composition of dust particles results in a negative SSA Ångström exponent.

Here, this method was applied for identification of dust events for the full time period from 2011 to 2021. The Ångström exponent of the SSA was calculated at a time resolution of $1\,\mathrm{h}$ from online wavelength-resolved scattering and absorption measurements at the JFJ. Scattering coefficients at three wavelengths ($450\,\mathrm{nm}$, $550\,\mathrm{nm}$, $700\,\mathrm{nm}$) were measured by an integrating nephelometer (3563, TSI, USA). Absorption coefficients at seven wavelengths ($370\,\mathrm{nm}$, $470\,\mathrm{nm}$, $520\,\mathrm{nm}$, $590\,\mathrm{nm}$, $660\,\mathrm{nm}$, $880\,\mathrm{nm}$, $950\,\mathrm{nm}$) were obtained from measurements of aethalometers (from 2011 to 2015: AE-31, Magee Scientific, Slovenia; from 2015 to 2021: AE-33, Magee Scientific, Slovenia). All calculations were carried out as detailed in Collaud Coen et al. (2004).

S1.3 Filtering of Saharan dust influenced composite samples based on optical flags and elemental ICP-MS data

While the optical flagging based on the Ångström exponent of the SSA provides a reliable way to detect Saharan dust influence at the JFJ, it offers no direct quantification of the event strength. For the pooled composite samples, short and weak episodes of Saharan dust during one sample day might not lead to a dominant chemical dust fingerprint. In addition, online optical flags are affected by periods of instrument downtime and detection sensitivity alters with instrument age.

Therefore, for filtering of Saharan dust influenced composite samples, titanium (Ti) ambient concentrations from Inductively Coupled Plasma Mass Spectrometry (ICP-MS) measurements of filters were utilized in combination with the optical flags as a more quantitative criterion. Ti was selected based on its largely homogeneous distribution in the Saharan dessert (Scheuvens et al., 2013), low background concentrations at the JFJ and reliable measurement above limits of quantification of the ICP-MS. A comparison of our dataset, showing different elements during Saharan dust episodes and reference background conditions, confirmed that Ti is one of the most reliable indicators for Saharan dust influence at the JFJ (Weng *et al.*, in preparation). A threshold Ti concentration for filtering Saharan dust dominated composite samples was defined (i.e. $0.002\,\mu\mathrm{g\,m^{-3}}$) utilizing the optical dust flags to find a balance in order to only filter out composite samples with dominating Saharan dust influence.

Figure S3a shows a time series of Ti ambient concentrations and Figure S3b a comparison of Ti and aluminum (Al) ambient concentrations, both colored by an optical Saharan dust flag criterion. Similar as Ti, Al is a reliable indicator for Saharan dust influence at the JFJ (while the data coverage above the limit of quantification is slightly lower). A threshold of $0.002\,\mu\mathrm{g\,m^{-3}}$ Ti for filtering Saharan dust influenced composite samples was defined. As illustrated in Figure S3a, the threshold assures that seasonal cycles of regional mineral dust are still retained, while strong long-range transported Saharan dust episodes are filtered out (cf. also optical flags in Figure S3b).

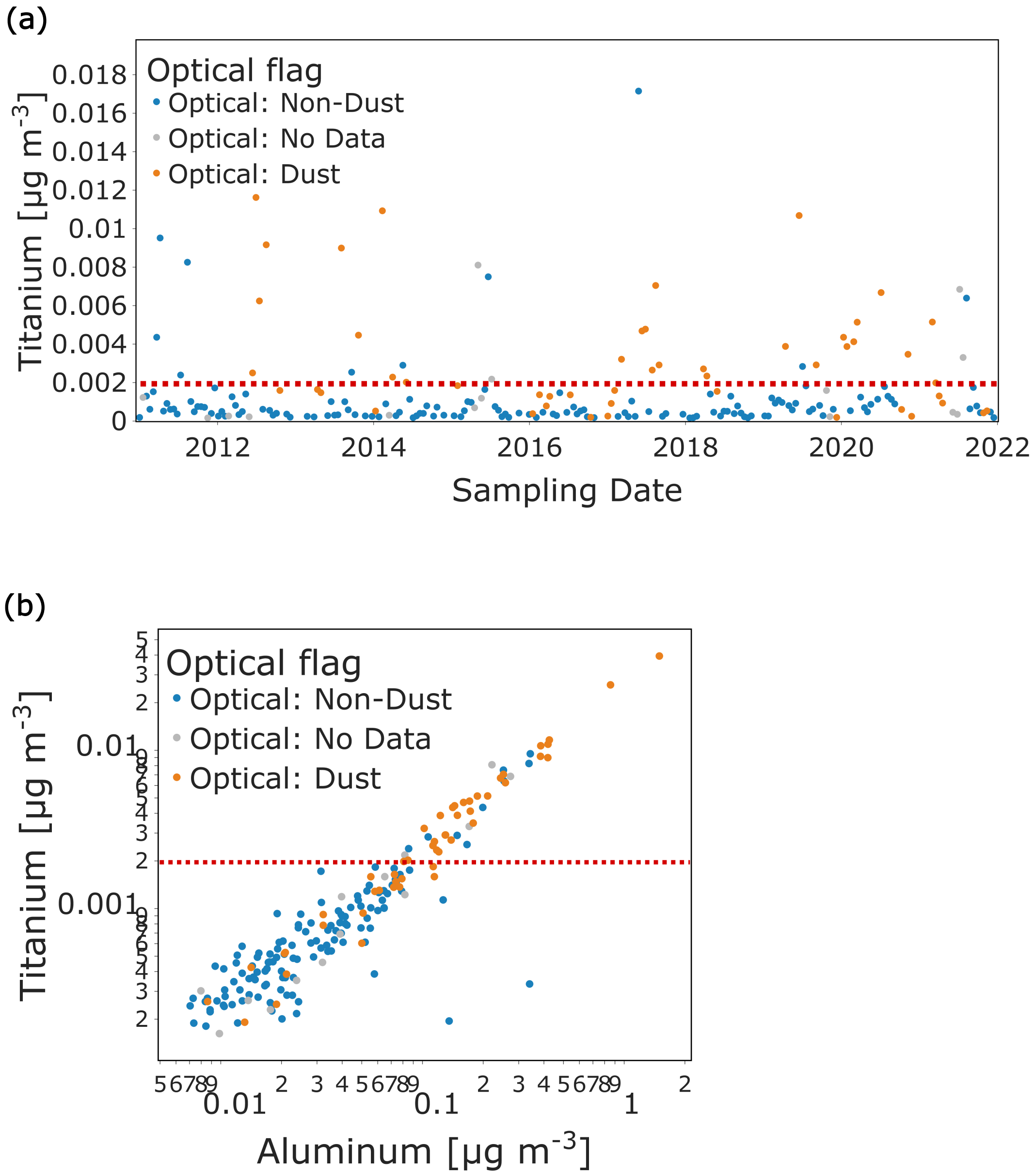

Figure S3. (a) Time series of Ti ambient concentrations at the JFJ, colored by optical Saharan dust flags. (b) Ti in comparison to Al ambient concentrations at the JFJ, colored by optical Saharan dust flags. 'Dust' (orange) means that composite sample contains at least one consecutive 12 h period of positive optical flag, 'No Data' (grey) describes periods of optical instrument downtime, i.e. when no optical flags are available. In both plots, the selected Ti threshold $0.002\,\mu\mathrm{g\,m^{-3}}$ for filtering samples as Saharan dust dominated is indicated by red dashed lines.

S2 Chemical analysis of filter samples

In the following, the chemical analysis and data processing steps for the different measurement techniques are described in detail. In section S3, measurements results of different independent analysis techniques (and sample preparation procedures) are compared for validation.

S2.1 Chemical analysis of bulk WSOC as well as non-target Offline-AMS and Offline-EESI-MS WSOA composition

S2.1.1 Sample Preparation

A single water extract of PM_{10} filters was used for analysis of water-soluble organic carbon (WSOC) by a total organic carbon (TOC) analyzer and bulk as well as near-molecular water-soluble organic aerosol (WSOA) composition by Offline-AMS and Offline-EESI-MS, respectively.

Circular filter punches of $14\,\mathrm{mm}$ diameter were submerged in $12\,\mathrm{mL}$ of ultrapure water (Milli-Q®, $<18.2\,\mathrm{M\Omega\,cm}$ at $25\,^{\circ}\mathrm{C}$, total organic carbon $< 5\,\mathrm{ppb}$, Merck Millipore, Germany) in extraction glass vials ($15\,\mathrm{mL}$ Pyrex Boro 3.3 with screw cap, Corning Incorporated, USA). In order to obtain analyte concentrations within the measurement range of the different instruments, 8 punches were pooled for Non-Dust samples and 4 punches for Dust samples. Extraction glass vials were then sonicated at $30\,^{\circ}\mathrm{C}$ for $20\,\mathrm{min}$, vortexed for $1\,\mathrm{min}$ and filtered through nylon membrane filters ($0.45\,\mathrm{\mu m}$ pore size, HPLC syringe filters YETI, Infochroma AG, Switzerland) into autosampler glass vials ($40\,\mathrm{mL}$, G075W-27/095-H, Infochroma AG, Switzerland). For filtration, polypropylene syringes ($10\,\mathrm{mL}$, single use syringes, Codan, Denmark) were used, after $4\times$ pre-conditioning of syringes and syringe filters with MilliQ. For each sample, the exact sample volume after extraction was determined gravimetricly by weighing autosampler glass vials with an electronic microbalance (NewClassic MF ML204, Mettler Toledo, Switzerland), before and after filling with extracts. This is necessary as some of the original extraction volume remains in syringes and filter punches, and exact volumes are required for subsequent quantification using an internal standard approach (volume loss ranged from $1\,\mathrm{mL}$ to $2.5\,\mathrm{mL}$). After filtration, all samples were spiked with a solution of $180\,\mathrm{\mu L}$ of $200\,\mathrm{\mu g\,mL^{-1}}$ ^{34}S-labeled ammonium sulfate (purity $\geq$ 90 %, Sigma-Aldrich, USA) and ^{15}N-labeled ammonium nitrate (purity 98.3 %, Sigma-Aldrich, USA). Besides the application in quantification of organic components, internal standard spiking fulfills additional purposes: Correction for nebulization instabilities and provision of carrier aerosol to ensure aerosol particle size distributions well in the efficient size windows of AMS and EESI-MS. Aliquots of $3\,\mathrm{mL}$ of the spiked extracts were used for quantification of WSOC, around $4\,\mathrm{mL}$ for analysis by Offline-AMS and Offline-EESI-MS.

S2.1.2 Quantification of WSOC by TOC analyzer

Quantification of WSOC was done by measurement of the water extracts with a TOC analyzer (TOC-L-series, Shimadzu, Japan). The TOC analyzer was run in its default non-purgeable organic carbon (NPOC) protocol. This protocol ensures removal of inorganic carbon (IC) constituents by acidification (HCl, H_3PO_4) of water extracts before measurement (Cui et al., 2024).

S2.1.3 Non-target chemical analysis by Offline-AMS and Offline-EESI-MS

For analysis of water-soluble organic compounds by Offline-AMS and Offline-EESI-MS, a combination of an autosampler (SC DX, Elemental Scientific, USA) and a nebulizer (APEX QW, Elemental Scientific, USA) was used to re-aerosolize sample water extracts using synthetic air as carrier gas. After passing through a Nafion® dryer (MD-070, Perma Pure, USA), aerosol was introduced to the AMS. The AMS combines flash vaporization ($\sim 600\,^{\circ}\mathrm{C}$) of aerosols with electron impact (EI) ionization (Jimenez et al., 2003). This allows for quantitative analysis of all non-refractory aerosol constituents. Yet, the high vaporization temperature and harsh ionization lead to extensive fragmentation of molecules before detection in the mass analyzer. The AMS was operated here with a mass resolution of ~ 3000 at m/z 120 and a m/z accuracy of $\leq 3\,\mathrm{ppm}$. Other operating principles and settings applied for the AMS were described in detail in previous studies (Daellenbach et al., 2016).

Before reaching the EESI-MS, the aerosol flow was additionally diluted $4\times$ with synthetic air to avoid strong reagent ion depletion in EESI-MS and therefore non-linear response for more polluted samples. A charcoal denuder was placed ahead of the EESI-MS for removal of gaseous contaminants, similar as in previous studies (Qi et al., 2020; Cui et al., 2024; Hao et al., 2025). In the EESI inlet, the aerosol gets extracted into charged electrospray droplets (Lopez-Hilfiker et al., 2019). The electrospray is generated from atomized reagent ion solution ($100\,\mu\mathrm{g}\,\mathrm{mL}^{-1}$ NaI in MilliQ®) in contact with a high-voltage power supply. In a heating capillary ($270\,^{\circ}\mathrm{C}$), droplets are vaporized leading to ionization by Coulomb explosions. Ions are detected with a atmospheric pressure inlet ToF-MS operated in positive ion mode. EESI being a very soft chemical ionization mechanism, sample molecules are usually detected intact, in the form of sodium adducts $[M + Na^{+}]$. The EESI-MS was operated with a resolution of ~ 8000 at m/z 200 and a m/z accuracy of $\leq 2\,\mathrm{ppm}$. Other operating principles and settings applied for the Offline-EESI-MS are identical to previous studies (Qi et al., 2020; Cui et al., 2024; Hao et al., 2025).

For both, AMS and EESI-MS, each extracted sample was measured in the following sequence: $8\,\mathrm{min}$ sample, followed by a $8\,\mathrm{min}$ period of MilliQ® water blank, followed by a $8\,\mathrm{min}$ period of internal standard spiked MilliQ® water (same spiking procedure as for samples), followed by a $12\,\mathrm{min}$ period of MilliQ® water blank.

S2.1.4 Data processing for Offline-AMS

Offline-AMS raw data was processed with ToF-AMS toolkits SQUIRREL (SeQUential Igor data RetRiEvaL v. 1.65F; D. Sueper, University of Colorado, Boulder, CO, USA) and PIKA (Peak Integration and Key Analysis v. 1.25F) for IGOR Pro (Igor 9, Wavemetrics Inc., USA). High resolution peak fitting was carried out from m/z 12-120, with a peak list consisting of overall 872 ions (including stable isotopes). The integrated ion signal intensity time series was then further processed using custom scripts in Python (Python 3.10.9, Python Software Foundation, 2022, https://www.python.org/). In short, the processing steps included the following:

- Outlier removal based on AMS N_2^+ signal (visual thresholding)
- Assignment of sample, spiked water and water blank periods to ion signal time series, based on times recorded by the autosampler control LabVIEW software (custom written VI, LabVIEW 2018, National Instruments, USA)

- Outlier filtering based on *median absolute deviation* approach with $^{15}NO_3^+$, applying a 3× deviation criterion
- Normalization of ion signals by internal standard ^{15}N signals, that is, sum of ^{15}NO and $^{15}NO_2$; using literature relative ionization efficiency (RIE) values for ^{15}N-nitrate ($RIE = 1$) and organics ($RIE = 1.4$), extract concentrations of ions i $conc_{extract}(i)$ in $\mu g\,mL^{-1}$ can be quantified by:

  $$conc_{extract}(i) = signal(i) * \frac{conc_{extract}(spike)}{signal(spike)} * \frac{RIE(spike)}{RIE(i)} \tag{S1}$$

  with the ion signal intensities for i $signal(i)$, spiked ^{15}N-nitrate mass concentrations $conc_{extract}(spike)$, ion signal intensities for spiked ^{15}N-nitrate $signal(i)$, and RIEs for the spiked ^{15}N-nitrate $RIE(spike)$, and ions i $RIE(i)$.
- Averaging of ion extract concentrations, based on assigned sample, spiked water, and water blank periods
- Correction of extract concentrations with the effectively weighed extract volumes after filtration and spiking, in comparison to the theoretical volumes initially used for extraction ($12\,mL$)
- For each sample, subtraction of its corresponding spiked water blank ion extract concentration
- Pieber correction for CO_2^+ and related ions, according to Pieber et al. (2016)
- Retrieval of AMS atomic ratios (O/C, N/C, S/C, H/C) and organic matter/organic carbon ratios (OM/OC), following the procedures of Aiken et al. (2007), and using the calibration factors of Aiken et al. (2008)
- Quantification of ambient mass concentrations $conc_{ambient}(i)$ in $\mu g\,m^{-3}$ for each ion i, using the following relationship:

  $$conc_{ambient}(i) = \frac{conc_{extract}(i) * V_{extraction}}{fraction_{filter}} * \frac{1}{V_{sampled\ air}} \tag{S2}$$

  with the extract concentrations of ions i $conc_{extract}(i)$ [$\mu g\,mL^{-1}$], extraction volumes $V_{extraction}$ [mL], fraction of extracted filter area of total filter area $fraction_{filter}$:

  $$fraction_{filter} = \frac{punch\ area * number\ of\ punches}{effectively\ sampled\ filter\ area} \tag{S3}$$

  and sampled air volume $V_{sampled\ air}$:

  $$V_{sampled\ air} = sampling\ time\ [h] * sampling\ rate\ [m^3 h^{-1}] \tag{S4}$$

- For each sample, subtraction of fieldblank hypothetical ambient mass concentrations (fieldblanks treated as samples in data analysis steps before)

For chemical composition analysis and Offline-AMS bulk atomic ratios, Offline-AMS ion filtering was performed on data to remove noisy ions. Threshold values were determined based on filter statistics, i.e. percentage of ions removed (per each AMS ion family) and total ion intensity fraction removed by filtering steps. For retrieval of bulk Offline-AMS WSOA, no ion filtering was performed. The following steps were carried out:

- Remove any stable isotope ions
- Remove ions that exhibit a negative intensity/concentration across $\geq 90\%$ of all samples
- Remove ions based on their intensity relative to water blank intensity (performed on sample and corresponding water blank data after averaging and before water blank subtraction): remove if ion not at least in $\geq 40\%$ of samples a factor of 3 higher in intensity than their corresponding water blanks
- Remove ions based on their intensity relative to fieldblank intensity (performed on sample and corresponding fieldblank data after water blank subtraction and before fieldblank subtraction): remove if ion not at least in $\geq 90\%$ of samples a factor of 1 higher in intensity than their corresponding fieldblanks

In this way, excluding stable isotope ions, 98 of in total 398 ions were removed (25%). Overall, around 93% of total ion concentration was retained.

S2.1.5 Data processing for Offline-EESI-MS

Offline-EESI-MS raw data were processed using the IGOR Pro (Igor 9, Wavemetrics Inc., USA) based software Tofware v4.0.3 (Tofwerk AG, Thun, Switzerland). A pre-averaging of raw data to $20\,\mathrm{s}$ intervals was done. High resolution peak fitting was carried out from m/z 100-380. The peak list consisted of overall 5001 ions (excluding stable isotopes), of which 3212 were clearly assigned of organic nature (carbon containing). MFAssignR was used to determine the chemical formula of initially unassigned peaks. The MFAssignR script was run for several samples of different seasonality. All unambiguously assigned peaks by MFAssignR were compared with the manually assigned peak list, one by one, and cross-checked with chemical databases. Similar to Offline-AMS data, Tofware exported time series were further processed with custom scripts in Python (Python 3.10.9, Python Software Foundation, 2022, https://www.python.org/). In short, the processing steps included the following:

- Outlier removal based on EESI-MS reagent ion related Na_2I^+ signal (visual thresholding)
- Assignment of sample, spiked water and water blank periods to ion signal time series, based on times recorded by the autosampler control LabVIEW software (custom written VI, LabVIEW 2018, National Instruments, USA)
- Outlier filtering based on *median absolute deviation* approach with Na_2I^+ signal, applying a $3\times$ deviation criterion

- Normalization of ion signals by primary ion Na_2I^+ signal
- Normalization of ion signals by sum of ^{34}S-Sulfate internal standard signals $Na_3[^{34}S]O_4^+$ and $Na_4[^{34}S]O_4I^+$
- Averaging of ion extract concentrations, based on assigned sample, spiked water, and water blank periods
- Correction of extract concentrations with the effectively weighed extract volumes after filtration and spiking, in comparison to the theoretical volumes initially used for extraction ($12\,\mathrm{mL}$)
- For each sample, subtraction of its corresponding spiked water blank ion extract concentration
- 'Semi-Quantification', i.e. correction of sample signal intensities with sampling and sample preparation parameters such as sampling rate, punch size, number of punches etc. identical to the quantification step for Offline-AMS (cf. Equation S2, Equation S3 and Equation S4); other than for Offline-AMS, for Offline-EESI-MS this step does not result in ion ambient concentrations due to the non-quantitative character of EESI-MS; however, it assures direct comparison of absolute signal intensities between samples with different sample preparation parameters (e.g. number of filter punches extracted)
- For each sample, subtraction of fieldblank signal intensities (fieldblanks treated as samples in data analysis steps before)

Calculation of Offline-EESI-MS atomic ratios $\frac{X}{C}$ (O/C, H/C, N/C) was done based on the ratio of ion signal intensities $Signal_i$ for each organic ion i weighted by the number of corresponding elements X or C $number_{X\ or\ C}$ contained in the molecular formula of that ion:

$$\frac{X}{C} = \frac{\sum_i (Signal_i * number_X)}{\sum_i (Signal_i * number_C)} \tag{S5}$$

Similar to Offline-AMS, ion filtering was performed to remove noisy ions. The following steps were carried out:

- Remove all Offline-EESI-MS ions that do not contain at least one carbon atom
- Remove ions based on their intensity relative to water blank intensity (performed on sample and corresponding water blank data after averaging and before water blank subtraction): remove if ion not at least in $\geq 40\%$ of samples a factor of 3 higher in intensity than their corresponding water blanks

In this way 719 of in total 3212 assigned organic ions were removed (22%).

S2.2 Analysis of major inorganic cations and anions as well as targeted chemical analysis of molecular organic tracers: (di-)carboxylic acids, sugars and sugar alcohols

Similar to previously reported standard protocols (Jaffrezo et al., 1998; Waked et al., 2014), a range of carboxylic and dicarboxylic acids were measured along with major inorganic anions and cations by Ion Chromatography-Mass Spectrometry (IC-MS). Additionally, a selection of sugars and sugar alcohols were quantified by a recently developed method based on Ultra High Performance Liquid Chromatography-Tandem Mass Spectrometry (UHPLC-MS/MS) (Bros et al., 2025).

S2.2.1 Sample Preparation for IC-MS and UHPLC-MS/MS

Details about materials and sample preparation procedures are provided in Bros et al. (2025). In short, 4 circular filter punches ($18\,\mathrm{mm}$) per sample were extracted by $6\,\mathrm{mL}$ of Milli-Q® and vortex-shaken for $20\,\mathrm{min}$. The extracts were then filtered through Milli-Q® pre-conditioned Ion Chromatography syringe filters ($0.2\,\mathrm{\mu m}$ pore size, Acrodisc, Cytiva, USA).

IC-MS analysis was carried out by direct injection of the filtrated aqueous extract. Before analysis with UHPLC-MS/MS, the filtrate was diluted 1:10 with acetonitrile containing $0.005\,\%$ NH_4OH and a mixture of three isotopically labeled internal standard sugars ($8\,\mathrm{ng\,mL^{-1}}$).

S2.2.2 Analysis by IC-MS

For IC-MS analysis, $1.5\,\mathrm{mL}$ of filtered extract was transferred into polypropylene vials. The analysis of organic acids was carried out using dual ion chromatography coupled to mass spectrometers. Inorganic anions and cations were detected by conductivity. For cations, an ion chromatography setup system (INTEGRION, Thermo Fisher Scientific, USA) was used configured with isocratic methanesulfonic acid (MSA) eluent and CG16-$4\,\mathrm{\mu m}$/CS16-$4\,\mathrm{\mu m}$ columns ($2\,\mathrm{mm}$, Thermo Fisher Scientific, USA). For anions and organic acids, a coupled IC-MS (INTEGRION and ISQ EC, Thermo Fisher Scientific, USA) system was used, configured with gradient KOH eluent and AG11HC-$4\,\mathrm{\mu m}$/AS11HC-$4\,\mathrm{\mu m}$ columns (2mm, Thermo Fisher Scientific, USA). The mass spectrometer was run in negative electrospray mode (–2700 V) and SIM mode tuned for each species with full scan and targeted detection. Procedural and analytical errors were lower than 10% for both methods. Limits of detection were below the $\mathrm{ng\,mL^{-1}}$ level in the samples for most of the compounds.

S2.2.3 Analysis by UHPLC-MS/MS

For UHPLC-MS/MS, a ultra-high-performance liquid chromatography setup (ExionLC AD binary pump, Sciex, USA) was coupled to a tandem mass spectrometer (5500 QTRAP, Sciex, USA). The chromatographic column applied was a Luna Omega Sugar HPLC column (Phenomenex, France) in combination with its corresponding guard column (SecurityGuard Cartridges, Phenomenex, France). The tandem mass spectrometer was run in negative electrospray ionization mode. The detailed instrument settings, measurement procedures and data analysis are described in Bros et al. (2025).

S2.3 Analysis of metal elemental composition

Major elements and trace metals were measured by ICP-MS.

S2.3.1 Sample Preparation for ICP-MS

A mild digestion was applied for dissolution of elements for analysis by ICP-MS. Mild mineralization of $6.2\,\mathrm{cm^3}$ of the quartz filter samples was carried out with strong ultra-trace metal grade acids without HF ($6\,\mathrm{mL}$ of 69% HNO_3, $3\,\mathrm{mL}$ of 37% HCl, 10 drops of concentrated H_2O_2) in a $22\,\mathrm{mL}$ pre-washed teflon reactor (Savillex, USA). The reactor was kept sealed for $24\,\mathrm{h}$ on a hot plate at $140\,^{\circ}\mathrm{C}$. After complete evaporation at $68\,^{\circ}\mathrm{C}$, samples were dissolved and transferred into metal free tubes with 2% HNO_3. Compared to a full mineralization with complete digestion of all elements using HF, the mild digestion has the advantage of a lower liability towards contaminations from the filter matrix. This is especially relevant for the samples from JFJ, where low ambient concentrations lead to low actual loadings of filter samples. The lower completeness of the mild digestion for a range of elements can to some extend be accounted for by comparison with recovery rates of measured reference materials, assuming similar behavior for the investigated samples.

S2.3.2 Analysis by triple quadrupole ICP-MS

Analysis of about 45 elements was carried out using a triple quadrupole ICP-MS (iCAP TQ ICPMS, Thermo Fisher Scientific, USA) coupled with an autosampler (SC4 DX, Elemental Scientific, USA) and FAST valve introduction. Analytical mode (SQ, or TQ-He / TQ-O2 / TQ-NH3) for each element was chosen according to Thermo Fisher Scientific library and matrix advice plus additional tests of interferences. Quantification was made by external calibration and isotopic dilution. Mineralization yields, analytical reproducibility and accuracy were verified using reference material (ERM-CZ120 fine dust and BCR-723 road dust, European Commission Joint Research Centre, Belgium), in-house mixed standard solutions, and certified solutions (CMS-5 and IV-STOCK50, Analab, France), respectively. Procedural and analytical errors were lower than 10% for metal elemental concentrations. The obtained metal concentrations were corrected for incomplete digestion by the recovery rates in Table S1.

Table S1. Recovery rates [%] for metals after mild digestion, obtained from analysis of certified reference materials.

Element	**Recovery (%)**
Na	60
Sc	64
Ti	46
V	69
Cr	64
Mn	78
Co	80
Cu	71
Zn	98
Ga	61
As	87
Rb	42
Sr	51
Y	74
Zr	14
Mo	81
Cd	81
Sb	64
Cs	62
Ba	65
La	74
Ce	70
Sm	78
Tb	60
Pb	87
Th	76
U	59

S3 Cross-validation of chemical analysis results

In order to validate analytical results of the different offline mass spectrometry techniques, a cross-validation was carried out. For this, ambient concentrations or relative intensities obtained from different instruments for overlapping analytes were compared.

S3.1 Offline-AMS and IC-MS inorganic sulfate

Sulfate was quantified in very good agreement by Offline-AMS and IC-MS. As all steps after the sampling were carried out independently for the two techniques (including the water extraction), the results also validate the sample preparation process.

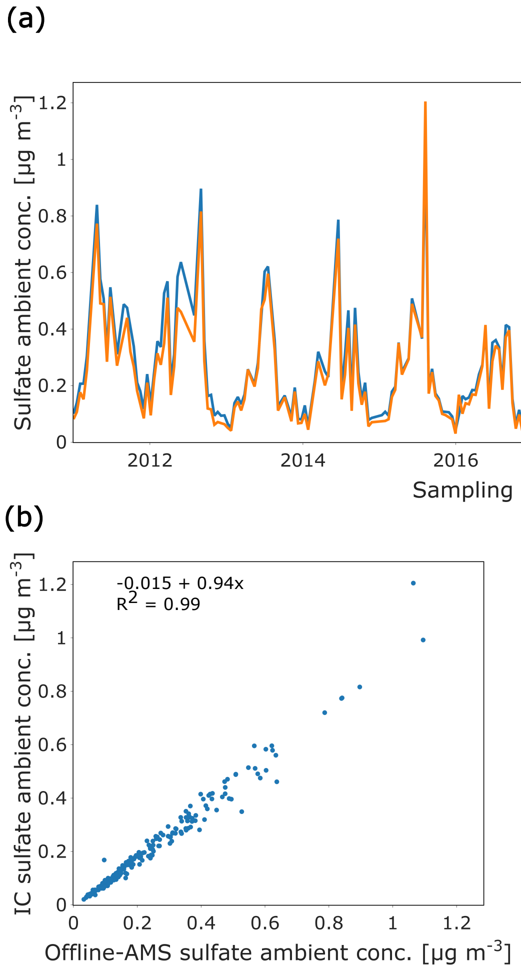

Figure S4. (a) Time series and (b) scatter plot of inorganic sulfate ambient concentrations obtained from Offline-AMS and IC-MS. In the scatter plot, the results of a linear fit and coefficient of determination (R^2) are provided.

S3.2 Offline-AMS and TOC analyzer WSOA

WSOA values quantified from Offline-AMS and the TOC analyzer (under consideration of Offline-AMS OM/OC-ratios) are very consistent. The small discrepancy for very low concentrations in some of the years is likely associated to instrument behavior, as sample preparation was equivalent for both techniques. Offline-AMS WSOA is more consistent with concentrations from previous online OA measurements at the JFJ (Fröhlich et al., 2015). One explanation for the discrepency of the TOC analyzer obtained WSOA can be the very low WSOC concentrations for fieldblank and winter samples, which could lie below the actual detection limits of the technique (e.g. inaccurate fitting of peak signals).

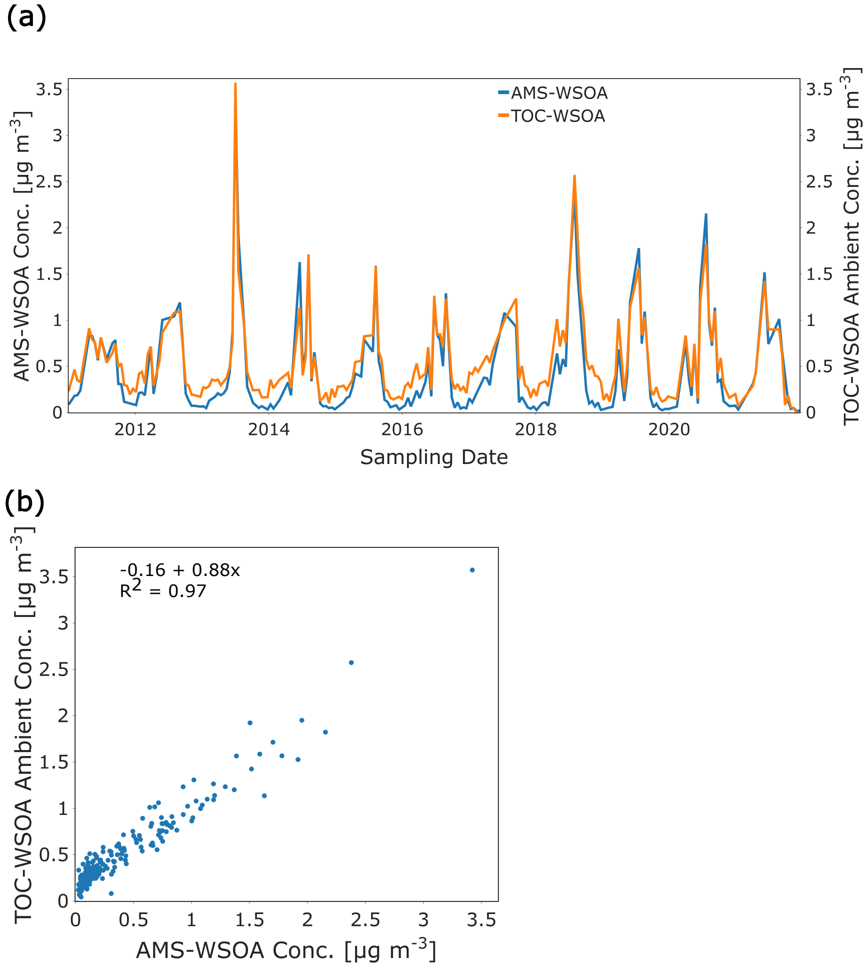

Figure S5. (a) Time series and (b) scatter plot of WSOA ambient concentrations obtained from Offline-AMS and the TOC analyzer (by multiplication of WSOC with Offline-AMS OM/OC ratios). In the scatter plot, the results of a linear fit and coefficient of determination R^2 are provided.

S3.3 Offline EESI-MS and IC-MS inorganic sulfate

Similar to Offline-AMS, sulfate was quantified in very good agreement by Offline-EESI-MS and IC-MS. This provides validation for Offline-EESI-MS as well as IC-MS and once more the sample preparation routines which were independent for the two techniques. At the same time consistency also between Offline-AMS and Offline-EESI-MS is demonstrated.

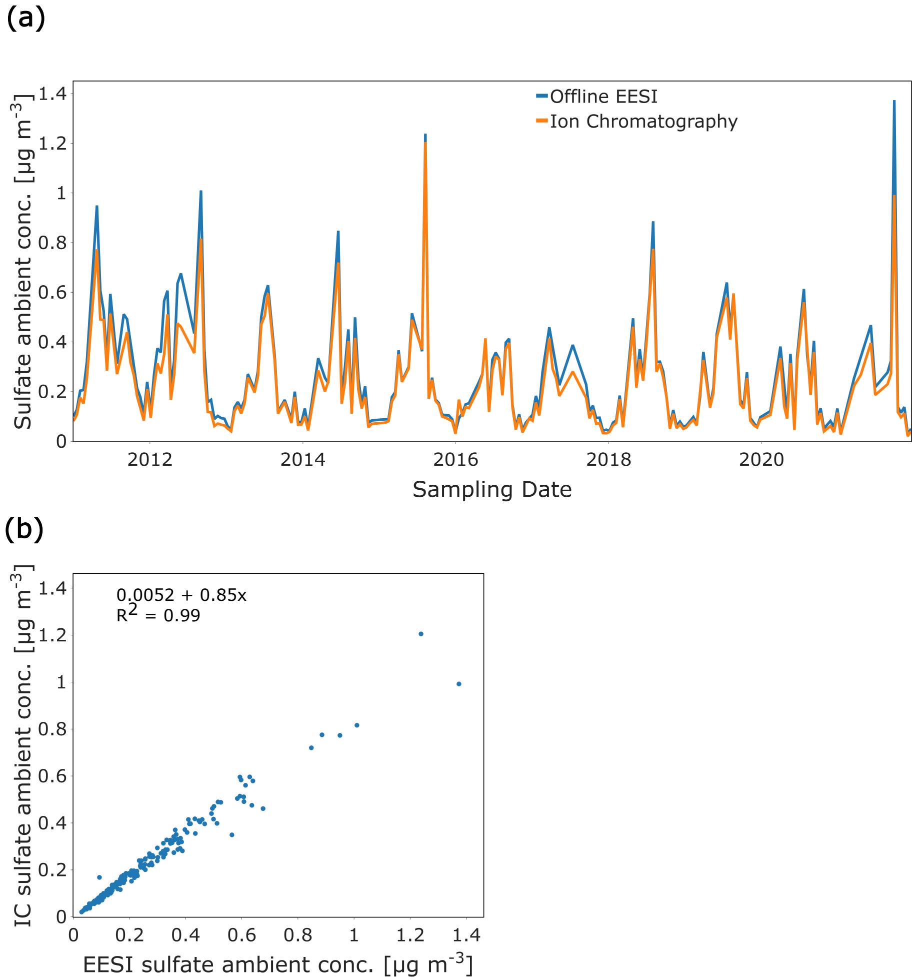

Figure S6. (a) Time series and (b) scatter plot of inorganic sulfate ambient concentrations obtained from Offline-EESI-MS and IC-MS. In the scatter plot, the results of a linear fit and coefficient of determination R^2 are provided.

S3.4 Offline-EESI-MS, IC-MS and UHPLC-MS/MS organic markers

Due to its non-target nature and strongly differing analyte sensitivities, the Offline-EESI-MS provides no direct absolute quantification for organic compounds. However, its near-molecular resolution allows comparison of relative signal intensities of sum formulas with respective quantified molecular resolution organic compounds from IC-MS and UHPLC-MS/MS. The presence of several isomers for a selected sum formula can complicate direct comparison for some species (especially those with low abundances and weak instrument sensitivities). Nevertheless, good agreements are found for a wide range of analytes from organic acids like oxalate and 3-MBTCA to sugar alcohols like 2-Methyltetrols.

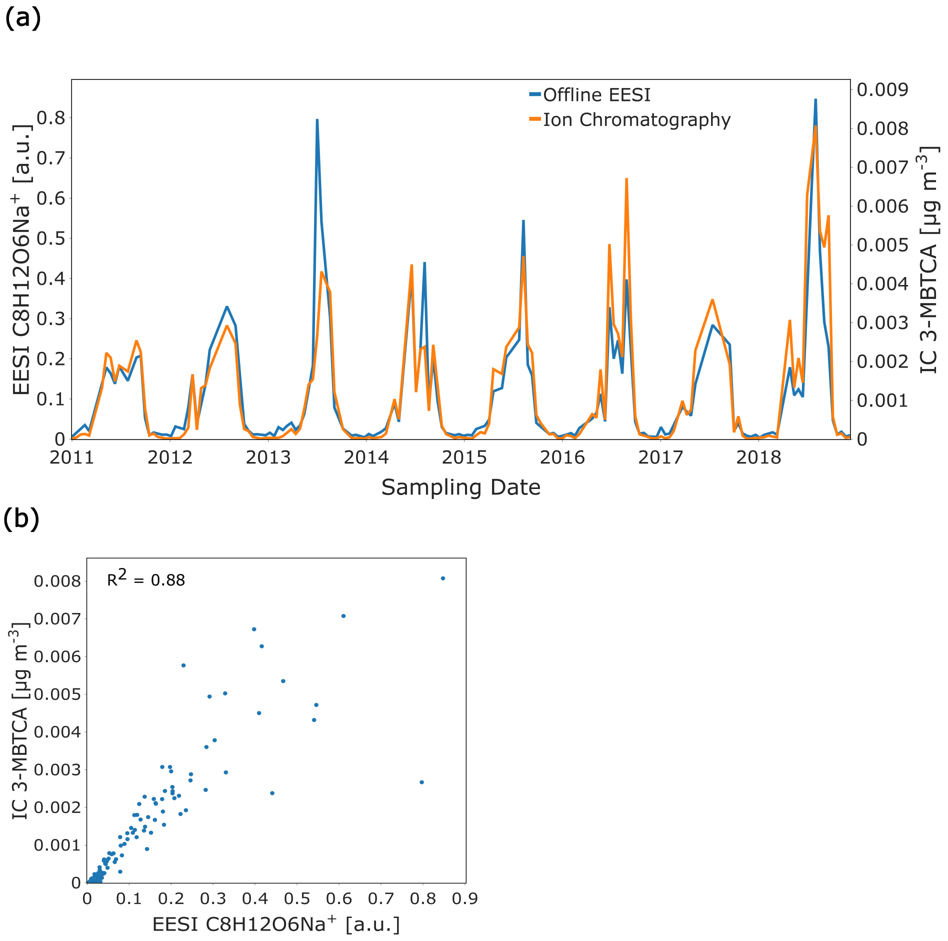

Figure S7. (a) Time series and (b) scatter plot of the relative signal intensity of the $C_8H_{12}O_6Na^+$ ion from Offline-EESI-MS and 3-methylbutane-1,2,3-tricarboxylic acid (3-MBTCA, $C_8H_{12}O_6$) ambient concentration obtained from IC-MS. In the scatter plot, the coefficient of determination R^2 is provided.

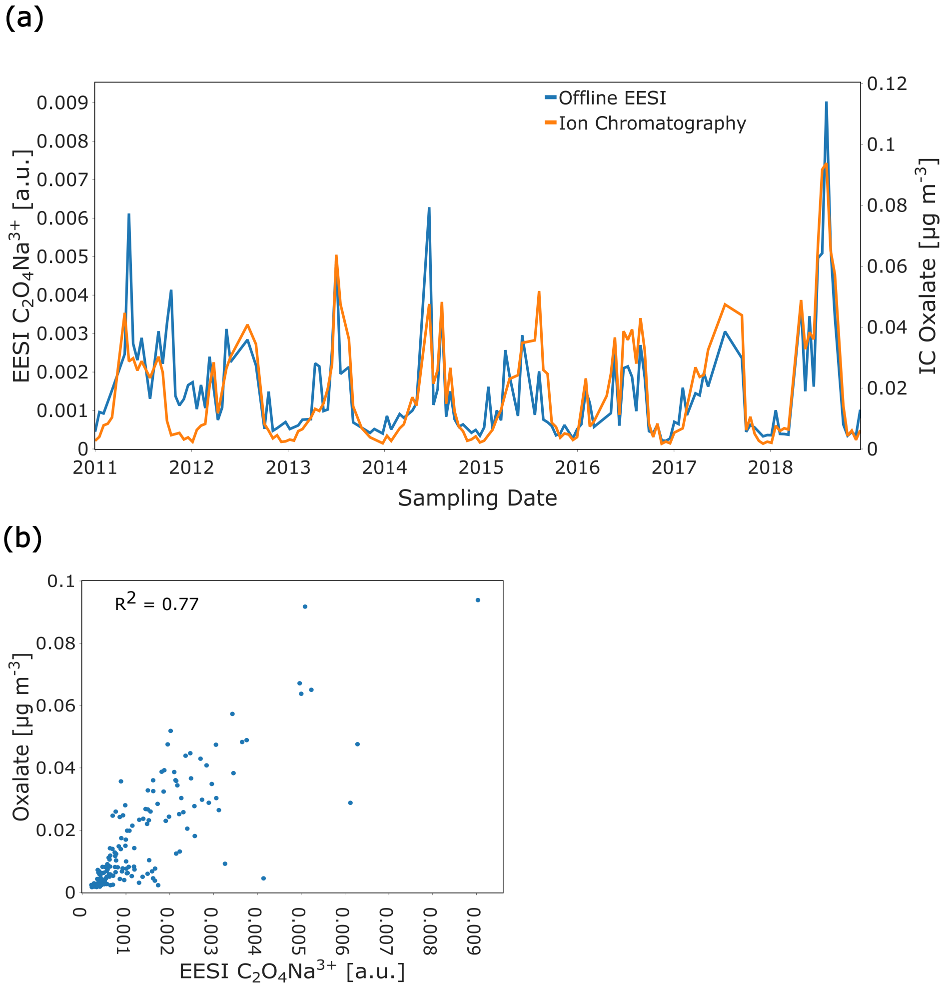

Figure S8. (a) Time series and (b) scatter plot of the relative signal intensity of the $C_2O_4Na^{3+}$ ion from Offline-EESI-MS and Oxalate $(C_2O_4^-)$ ambient concentration obtained from IC-MS. In the scatter plot, the coefficient of determination R^2 is provided.

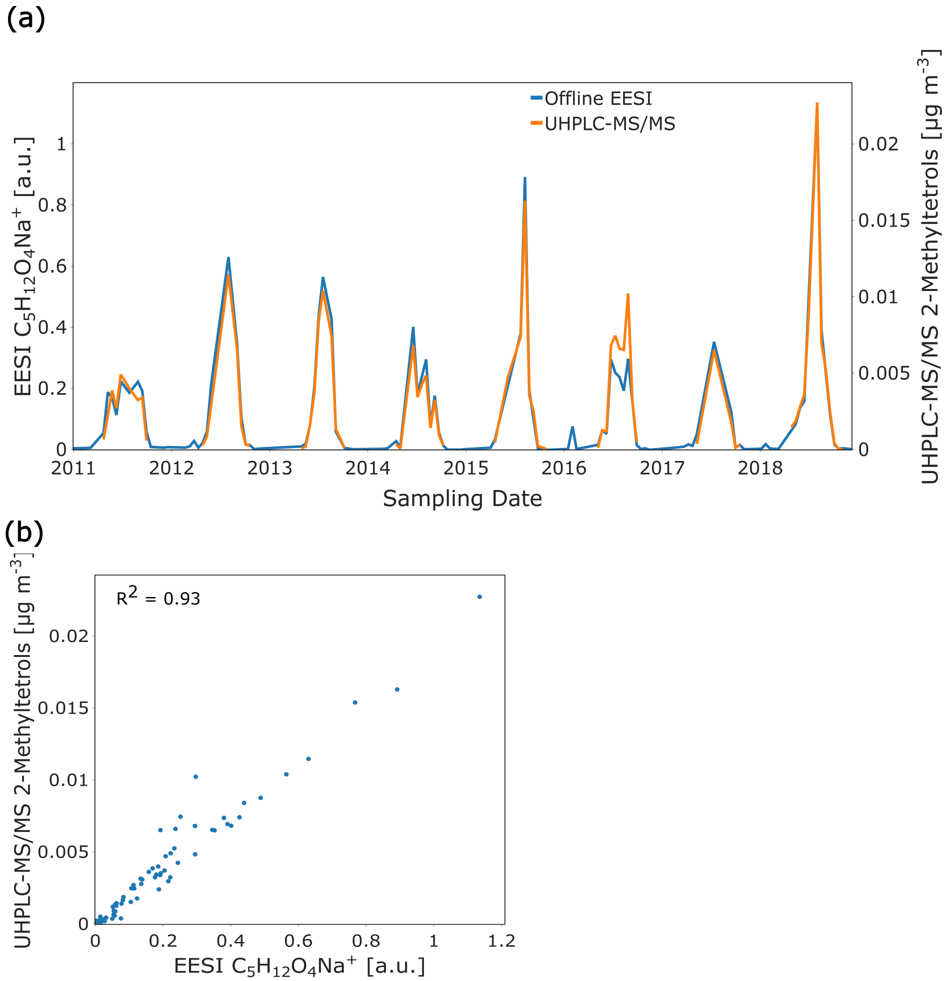

Figure S9. (a) Time series and (b) scatter plot of the relative signal intensity of the $C_5H_{12}O_4Na^+$ ion from Offline-EESI-MS and 2-Methyltetrols ($C_5H_{12}O_4$) ambient concentration obtained from UHPLC-MS/MS. In the scatter plot, the coefficient of determination R^2 is provided.

S4 Online measurement of PM_1 and PM_{10} mass concentrations at the JFJ and referencing to gravimetric PM_{10}

Since October 2016, online PM_1 and PM_{10} mass concentrations were measured by a fine dust monitor (FIDAS 200, PALAS, Germany) at the JFJ. The FIDAS PM_1 and PM_{10} concentrations are obtained from single-particle optical scattering measurements which allow estimation of aerosol size distributions (and, with further assumptions, calculation of mass concentrations). The lower size bin limit lies at $0.18\,\mu\mathrm{m}$.

The FIDAS provides high time resolution measurements of PM_1 and PM_{10}. The European reference method for determination of different PM levels is however gravimetric measurement (European Committee for Standardization (CEN), 2023). As the optical determination of the FIDAS differs conceptually strongly from gravimetric measurements, FIDAS PM_{10} is compared to gravimetric PM_{10} and corrected for accordingly. There are no gravimetric PM_1 measurements at the JFJ. Therefore, correction factors of PM_{10} are applied also to PM_1, which can lead to higher uncertainties in FIDAS PM_1 levels.

Figure S10a shows a comparison of gravimetric PM_{10} and FIDAS PM_{10}. A very good relative agreement is obtained for the two independent methods. The mismatch in absolute concentrations originates mostly from the FIDAS raw data being recorded under normal conditions assuming ambient pressures of $1013\,\mathrm{mbar}$ (the air-volume ratio between $653\,\mathrm{mbar}$ and $1013\,\mathrm{mbar}$ is approximately 1.55). For correction, the slope of a simple linear regression (1.7 as shown in Figure S10a was applied for both FIDAS PM_1 and PM_{10}.

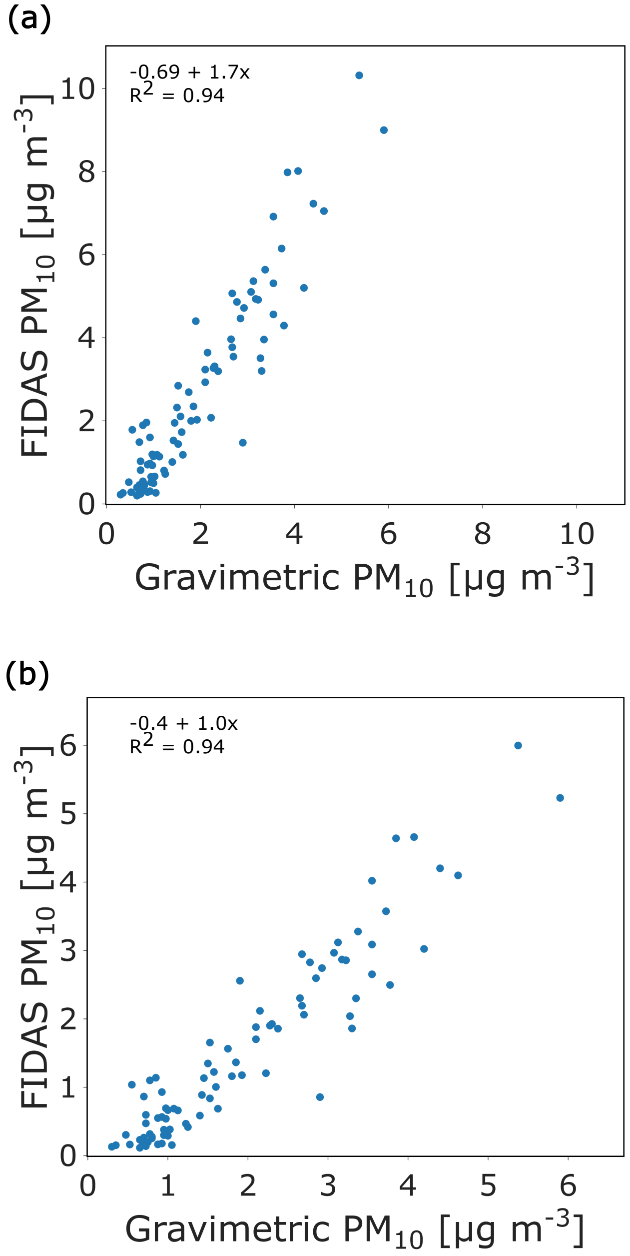

Figure S10. (a) FIDAS PM_{10} uncorrected data as a function of gravimetric PM_{10}. (b) FIDAS PM_{10} after correction with linear regression slope of (a) as a function of gravimetric PM_{10}.

S5 Online measurement of eBC at the JFJ and comparison to thermal-optical EC

Equivalent black carbon (eBC) concentrations were obtained from online aerosol absorption measurements. For this, a multi-angle absorption photometer (MAAP, 5012, Thermo Fisher Scientific, USA) was run at the JFJ, measuring aerosol absorption coefficients at effectively $637\,\mathrm{nm}$. Absorption data were processed according to Müller et al. (2011) and the multi-site harmonized mass absorption cross-section (MAC) of $10\,\mathrm{m}^2\,\mathrm{g}^{-1}$ was applied for conversion to eBC concentrations, in line with the current eBC L3 *Aerosol, Clouds and Trace Gases Research Infrastructure* (ACTRIS) calculation procedure.

Figure S11 shows a comparison of retrieved eBC concentrations and thermal-optical EC for overlapping time periods. The concentrations follow a clear linear trend above $50\,\mathrm{ng}\,\mathrm{m}^{-3}$, while higher discrepancies are observed for low concentrations. This could be explained by values close to the limits of quantification of both methods. As shown by the linear fit results in Figure S11, there is a factor difference between eBC and EC that corresponds to about $15\,\%$ surplus of eBC. Discrepancies at higher concentrations could be related to a not perfectly adequate site specific MAC value especially under conditions with high OA concentrations, through lensing effects by organic coatings on black carbon (Zhang et al., 2018; Motos et al., 2020). As the eBC and EC mass concentration fraction of PM_{10} is negligibly low at the JFJ and mostly the relative concentrations are of interest in this work, no correction between the two methods is applied.

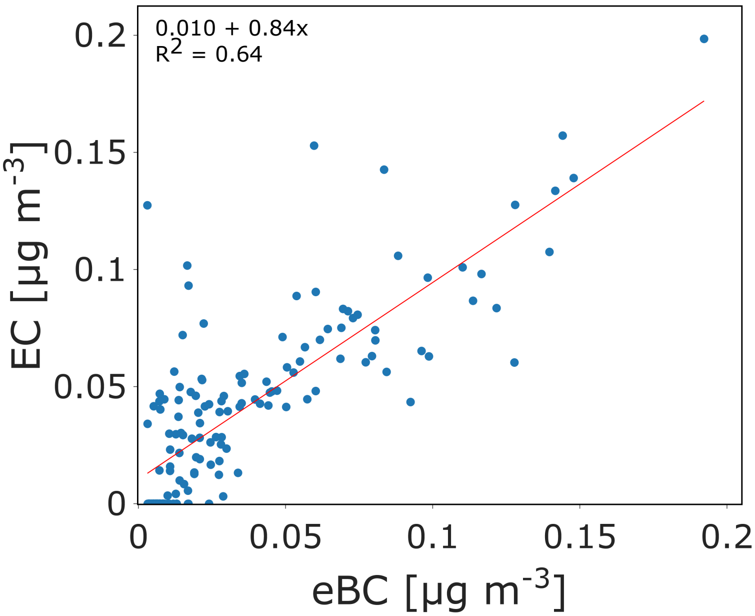

Figure S11. Comparison of thermal-optical EC and optical eBC ambient concentrations at the JFJ. Data is from the periods of August 2013 to September 2014 and March 2019 to November 2019 (daily filter sample EC and eBC averaged accordingly). In the scatter plot, the results of a linear fit and coefficient of determination R^2 are provided.

S6 Online *in-situ* measurements of different trace gases at the JFJ

S6.1 Measurement of nitrogen oxides NO, NO_2 and NO_x

Nitrogen monoxide (NO) was measured by a chemiluminescence detector (CLD 89p, Eco Physics, Switzerland). The sum of nitrogen oxides NO_X ($= NO + NO_2$) was quantified by a Correct Analysis of NO_X (CRANOX) system. The CRANOX systems consists of a photolysis converter (PLC 762, ANNOx, UK) and a chemiluminescence NO monitor (CLD 89p, Eco Physics, Switzerland). The photolysis converter selectively converts NO_2 to NO. Cross selectivity towards NH_3 and HNO_3 are below $0.1\,\%$, for peroxyacetyl nitrate (PAN) below $5\,\%$ and for HNO_2 below $20\,\%$. As the reduction of NO_2 to NO in the converter is not quantitative, a conversion efficiency was regularly determined (3 days) by zero air and calibration gas. Separate NO_2 values can subsequently be retrieved by calculation of the difference of NO_X and the independently measured NO.

S6.2 Measurement of ozone

Ozone (O_3) was measured by a photometric O_3 analyzer (until July 2011: 49C, from July 2011: 49i, Thermo Fisher Scientific, USA) based on UV absorption (peak at $254\,\mathrm{nm}$).

S6.3 Measurement of sulfur dioxide

Sulfur dioxide (SO_2) was measured by a SO_2 analyzer (until October 2011: 43C TL, from October 2011: 43i TLE, Thermo Fisher Scientific, USA) based on UV fluorescence.

S7 Semi-continuous online measurement of VOCs by Medusa cold trap gas-chromatography mass spectrometry

Medusa cold trap gas-chromatography mass spectrometry (Medusa GC-MS) was applied for semi-continuous measurement of a range of non-methane hydrocarbons and halogenated VOCs at the JFJ. Medusa consists of a cold-trap pre-concentration setup (Miller et al., 2008). In short, $2\,\mathrm{L}$ ambient air samples are pre-concentrated on a cold trap ($-165\,°\mathrm{C}$), cryo-distilled and focused on another cold trap. There, major air constituents N_2, O_2, H_2O, CO_2 and noble gases are removed, after which the analytes are transferred to the GC unit for separation and quadrupole MS (Agilent 5973, Agilent Technologies, USA) for detection. Measurement cycles are $1\,\mathrm{h}$, followed each by a $1\,\mathrm{h}$ calibration run with measurement standards to account for instrumental drifts.

S8 Measurement of meteorological parameters and calculation of the humidity ratio ω

S8.1 Measurement of meteorological parameters at the JFJ

Meteorological measurements at the JFJ were conducted by the federal office of meteorology and climatology (MeteoSwiss) as part of their SwissMetNet network at a $10\,\mathrm{min}$ time resolution (Appenzeller et al., 2008). Temperature and realtive humidity (RH) were measured by a heated weather station with a dew point mirror (Thygan, Meteolabor, Switzerland). Barometric pressure was recorded by a digital barometer (PTB220, Vaisala, Finland). Global solar radiation was measured by pyranometer (CM21, Kipp & Zonen B.V., Netherlands). For comparison to lower time resolution chemical data, averages of the meteorological parameters for the composite filter sample periods were calculated.

Figure S12 presents seasonalities of temperature, RH and barometric pressure at the JFJ.

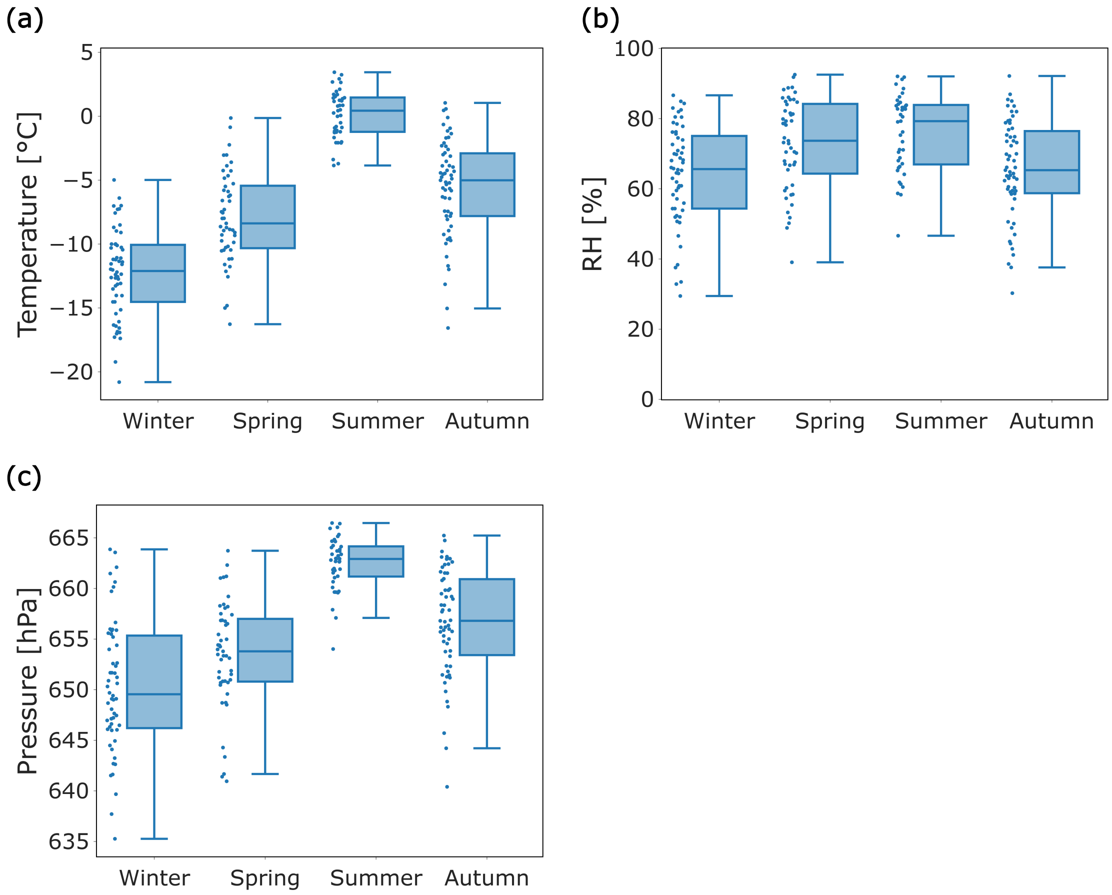

Figure S12. Seasonal variability of (a) Temperature, (b) RH and (c) barometric pressure. Depicted are averages of high time resolution data for the same time periods as the composite filter samples analyzed in this study. Seasons are defined as Winter - DJF, Spring - MAM, Summer - JJA, Autumn - SON.

S8.2 Calculation of the humidity ratio ω and seasonal comparison to other variables impacting OH radical production

Humidity ratios (ω) of the air masses at the JFJ were calculated from temperature, RH and barometric pressure. In a simplified approach, it was assumed that no metastable thermodynamic states like supercooled liquid water are relevant. First the saturation vapor pressure of water was estimated using the parameterization introduced by Buck (valid from $-80\,^{\circ}\mathrm{C}$ to $50\,^{\circ}\mathrm{C}$) (Buck, 1981). As the saturation vapor pressure differs for liquid water and ice, Buck applies two separate equations depending on temperature (above or below $0\,^{\circ}\mathrm{C}$):

$$e_w = 6.1121 * \exp\left(\frac{17.502T}{240.97+T}\right) \tag{S6}$$

$$e_i = 6.1115 * \exp\left(\frac{22.452T}{272.55+T}\right) \tag{S7}$$

where T is temperature, e_w and e_i are the saturation vapor pressures with respect to liquid water ($T \geq 0$ °C) and ice ($T < 0$ °C), respectively.
With the calculated water saturation vapor pressures, the actual water vapor partial pressure e can be calculated using the RH:

$$e = \frac{RH}{100} * e_w \tag{S8}$$

$$e = \frac{RH}{100} * e_i \tag{S9}$$

Then, ω can then be retrieved using the barometric pressure p:

$$\omega[g/kg] = 0.622 * \frac{e}{p-e} * 1000 \tag{S10}$$

where the factor 0.622 is the ratio of molecular weights of water vapor to dry air (Wallace and Hobbs, 2006) and 1000 is the conversion factor of [kg/kg] to [g/kg].

Figure S13 shows the relationship between ω, temperature and RH. The impact of temperature on the saturation vapor pressure overall dominates the magnitude of ω, while RH can introduce considerable variability for comparable temperature regimes.

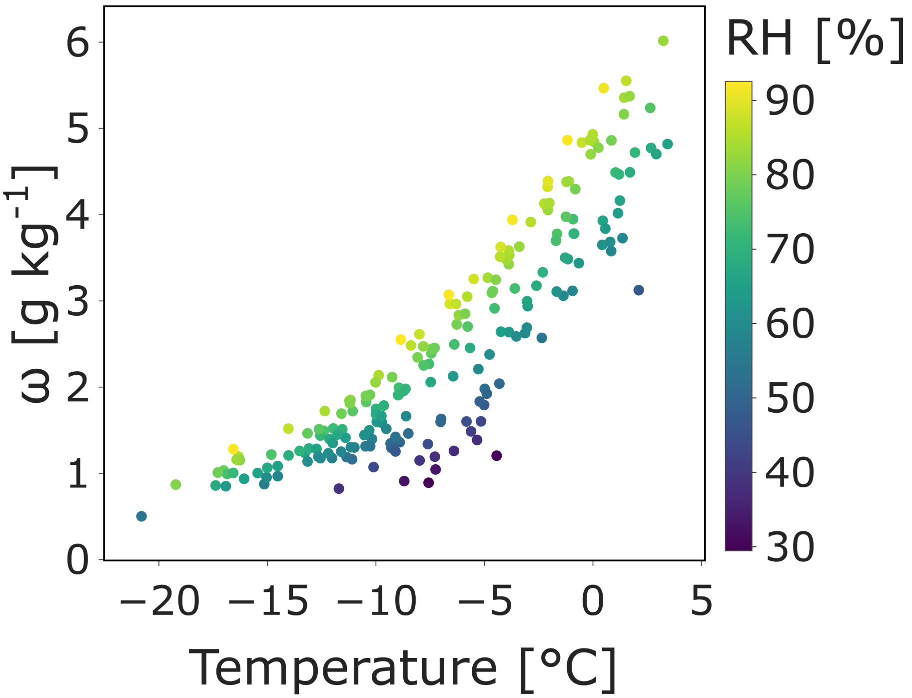

Figure S13. ω as a function of temperature at the JFJ, colored by RH. Depicted are averages of high time resolution data for the same time periods as the composite filter samples analyzed in this study.

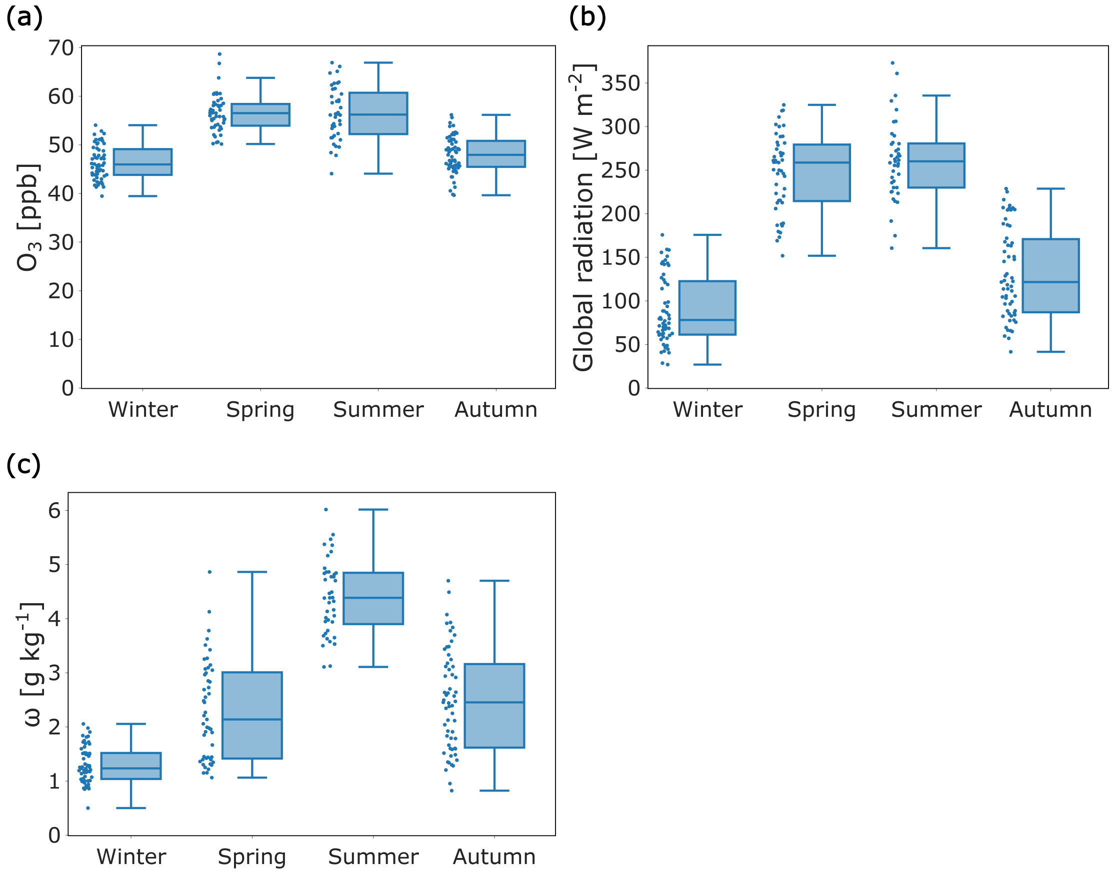

Figure S14. Seasonal trends of (a) ozone mixing ratios, (b) global solar radiation and (c) ω at the JFJ. Depicted are averages of high time resolution data for the same time periods as the composite filter samples analyzed in this study. Seasons are defined as Winter - DJF, Spring - MAM, Summer - JJA, Autumn - SON. Sampling dates dominated by Saharan dust were omitted from all plots.

S9 Measurement of different PBLi tracers and comparison with the humidity ratio ω

S9.1 Online measurement of PBLi tracers

Three independent PBLi tracers were measured online *in-situ* at the JFJ: i) NO_y/CO [ppb/ppb], the ratio of the sum of reactive nitrogen species (NO_y) and carbon monoxide (CO), ii) ^{222}Rn, the concentrations of radon-222 and iii) N_{90}, the number concentration of accumulation mode particles above $90\,\mathrm{nm}$. A detailed description of the performances of the different PBLi tracers, also with respect to independent transport simulations by the Lagrangian transport and dispersion model FLEXPART, is provided in Herrmann et al. (2015).

The sum of reactive nitrogen species NO_y was measured by a NO chemiluminescence detector (CLD 89p, Eco Physics, Switzerland) after conversion of reactive nitrogen compounds to NO on a heated gold catalyst ($300\,°\mathrm{C}$) with $2\,\%$ CO as reducing agent (Zellweger et al., 1999, 2000; Pandey Deolal et al., 2012). Due to the transformation to NO in the measurement setup, NO_y is reported as mixing ratios (of measured NO), even though NO_y is an integrated parameter over a range of species (both gas and particle phase). Measurements were discontinued in February 2020. Carbon monoxide CO was measured by cavity ring down spectroscopy (G2401, Picarro, USA) since 2012. Before 2012, the measurement was based on nondispersive infrared absorption (APMA 360 and APMA 370, Horiba, Japan).

^{222}Rn was monitored using a setup based on a two-filter dual flow loop design (Whittlestone and Zahorowski, 1998) in combination with a $750\,\mathrm{L}$ ^{222}Rn detection chamber described in detail by Griffiths et al. (2014). Due to local construction activities and changes in the ventilation system in proximity to the ^{222}Rn setup, data from January 2013 to October 2015 were omitted.

N_{90} was inferred from aerosol size distributions measured by a scanning mobility particle sizer (SMPS). A custom build SMPS was used, consisting of a ^{85}Kr bipolar diffusion charger, a custom modified differential mobility analyzer (DMA, TSI 3071, USA) and a condensation particle counter (CPC, TSI 3775, USA) (Wiedensohler et al., 2012; Herrmann et al., 2015). A size range of $10\,\mathrm{nm}$ to $450\,\mathrm{nm}$ was covered.

A time series of the three different PBLi tracers, averaged for the same time periods as the analyzed filter samples, is presented in Figure S15. The seasonalities of PBLi tracers are depicted in Figure S16.

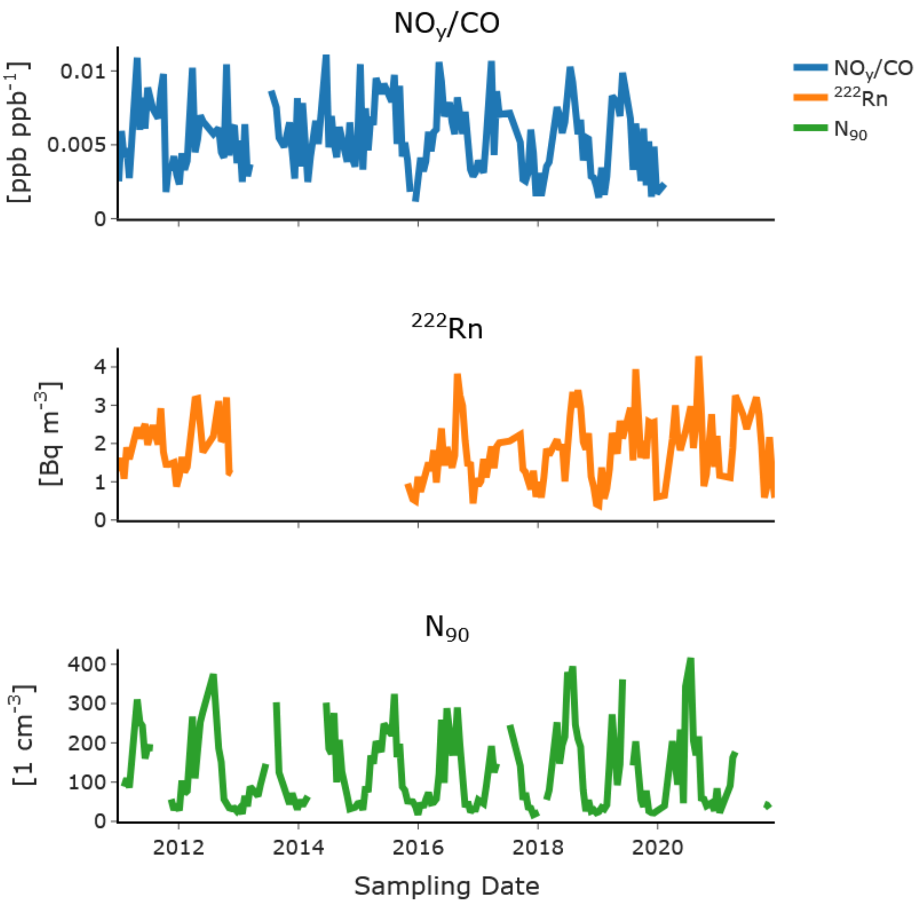

Figure S15. Time series of the different PBLi tracers NO_y/CO, ^{222}Rn and N_{90} measured at the JFJ from 2011 to 2021. Depicted are averaged data for the same time periods as the composite samples chemically analyzed in this study. Sampling dates dominated by Saharan dust were omitted from all plots.

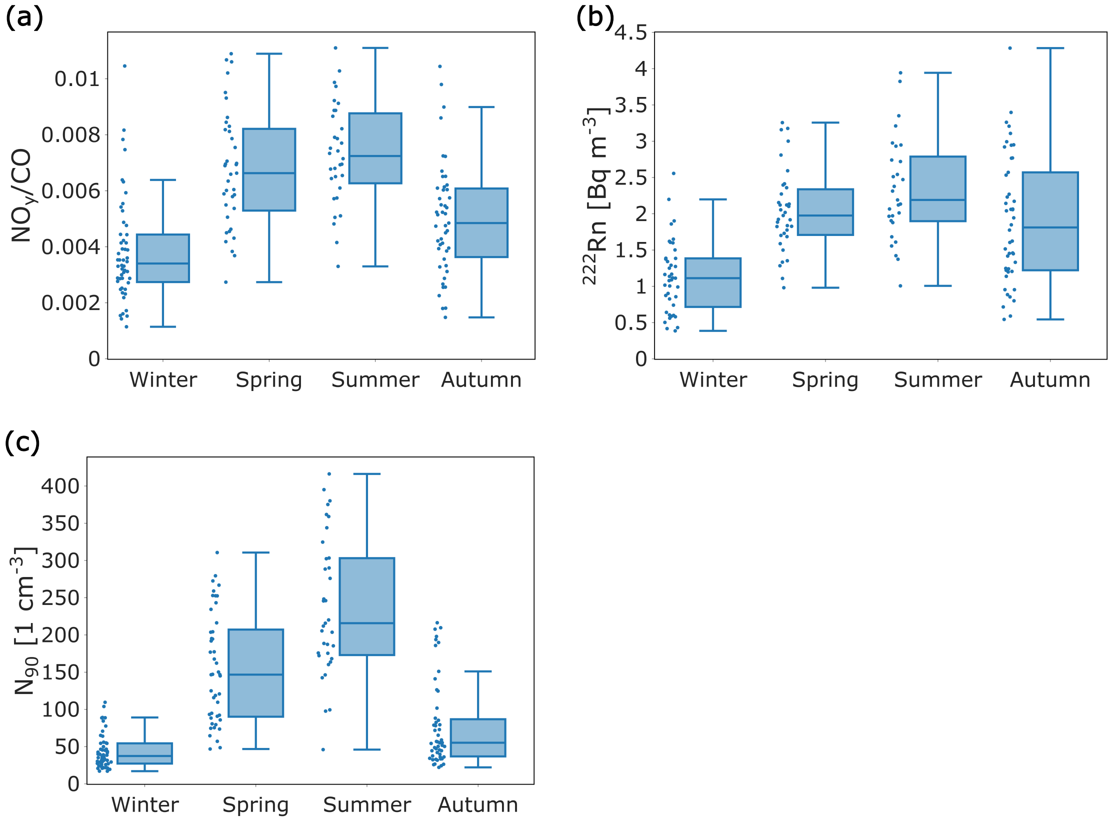

Figure S16. Seasonal trends of different PBLi tracers: (a) NO_y/CO, (b) ^{222}Rn and (c) N_{90}. Depicted are averaged data for the same time periods as the composite samples chemically analyzed in this study. Seasons are defined as Winter - DJF, Spring - MAM, Summer - JJA, Autumn - SON. Sampling dates dominated by Saharan dust were omitted from all plots.

S9.2 Evaluating the relationship of ω and PBLi

In order to disentangle the effects of PBLi and atmospheric oxidative capacity histories of air masses, the behavior of ω with respect to PBLi tracers is characterized. Figure S17 shows the relationship of ω and the PBLi tracer NO_y/CO at the JFJ, colored by the different PBL associated species ^{222}Rn, NO_x and NO_y. Analogously, Figure S18 shows the same relationship with respect to eBC and tetrachloroethylene (C_2Cl_4). These species are all strongly associated to originate from emission sources in the PBL (cf. Griffiths et al. (2014) for ^{222}Rn, Zellweger et al. (2000) for NO_x and NO_y, Baltensperger et al. (1997) for eBC and Figure S20 for C_2Cl_4).

On one side, a correlation of ω with NO_y/CO can be observed, in the sense that high levels of ω are almost exclusively found for moderate or high NO_y/CO. This can be explained by the fact that the atmospheric water vapor originates mainly from surface evaporation in the PBL (Jin et al., 2024). Therefore elevated ω at high altitudes is bound to intrusions of air masses with recent contact to the earth's surface (as indicated by high NO_y/CO). On the other side, the scatter plots clearly show that there is a range of conditions with strong PBLi but only low or moderate ω. This is firstly illustrated by the relationship of ω and NO_y/CO. Secondly, it is confirmed by all the species associated to PBL origin in Figure S17 and Figure S18. For low ω and NO_y/CO, these species show low levels (as PBLi are low). For high NO_y/CO, i.e. strong PBLi, they show generally increased levels, essentially covering the whole range of ω. The purely gas-phase species NO_x and C_2Cl_4 additionally feature a clear trend for depletion under high ω. Their mixing ratios are strongly bound to transport from the PBL on the one side and oxidative degradation on the other, highlighting the role of ω for the atmospheric oxidative capacity history of PBLi air masses at the JFJ.

In the following, a statistical validation of the described relationships is provided in two ways. Central to this analysis is to quantitatively demonstrate that ω exhibits not only substantial variability but in some cases particularly low levels even under strong PBLi.

Firstly, Figure S19 shows box plots of the PBL associated species of Figure S17 and Figure S18 for low ω under weak and strong PBLi conditions (as represented by NO_y/CO). Threshold values of $\leq 3\,\mathrm{g\,kg^{-1}}$ for ω and ≤ 0.005 for NO_y/CO were applied. To make this comparison robust, the data in the two categories $'Low\ NO_y/CO,\ Low\ \omega'$ and $'High\ NO_y/CO,\ Low\ \omega'$ were re-sampled to a subset with identical median ω. The p-values of Mann-Whitney-U-tests (depicted in the plots) show that all PBL associated species are significantly elevated for the $'High\ NO_y/CO,\ Low\ \omega'$ case. As data are resampled to equal median ω (so there is no significant difference in ω for the two categories), this proves the statements made above.

Another statistical robust validation is provided by a quantile regression for ω with the two PBLi tracers NO_y/CO and ^{222}Rn as predictors. Three different regression models were run:

- A median (q = 0.5) quantile regression:

$$\omega = \beta_0 + \beta_1\,\mathrm{NO_y/CO} + \beta_2\,{}^{222}\mathrm{Rn} \tag{S11}$$

- A lower-tail (q = 0.1) quantile regression:

$$\omega_{0.1} = \beta_0 + \beta_1 \, \mathrm{NO_y/CO} + \beta_2 \, {}^{222}\mathrm{Rn} \tag{S12}$$

- A lower-tail (q = 0.1) quantile regression including an interaction term of NO_y/CO and ^{222}Rn.:

$$\omega_{0.1} = \beta_0 + \beta_1 \, \mathrm{NO_y/CO} + \beta_2 \, {}^{222}\mathrm{Rn} + \beta_3 \left(\mathrm{NO_y/CO} \times {}^{222}\mathrm{Rn}\right) \tag{S13}$$

At a median level, ω increases with both predictors as indicated by the positive coefficients β for NO_y/CO ($\beta = 189.2$, at $95\,\%$ confidence interval, p $<$ 0.001) and for ^{222}Rn ($\beta = 0.5$, at $95\,\%$ confidence interval, p $<$ 0.001). At the 10th percentile, both predictors remain statistically significant, however their effects are markedly reduced: NO_y/CO ($\beta = 58.3$, at $95\,\%$ confidence interval, p $<$ 0.001) and ^{222}Rn ($\beta = 0.27$, at $95\,\%$ confidence interval, p $<$ 0.001). This indicates that their ability to raise the lower tail of the ω distribution is limited. Moreover, the model including the interaction term reveals a significant negative joint effect ($\beta = -20.2$, at $95\,\%$ confidence interval, p = 0.004), while the main effects remain positive. This indicates that even when both predictors (i.e. PBLi tracers) are large, ω can remain low.

In conclusion, the plots and statistical evaluation make clear that high PBLi is conditional for high ω. Yet, high ω is not exclusive at high or moderate PBLi, where a broad distribution of ω is observed. The broadness of this distribution allows for an independent investigation of meteorological transport (proxy: NO_y/CO or ^{222}Rn) and atmospheric oxidative capacity (proxy: ω) impacts on gas and aerosol loadings observed at the JFJ.

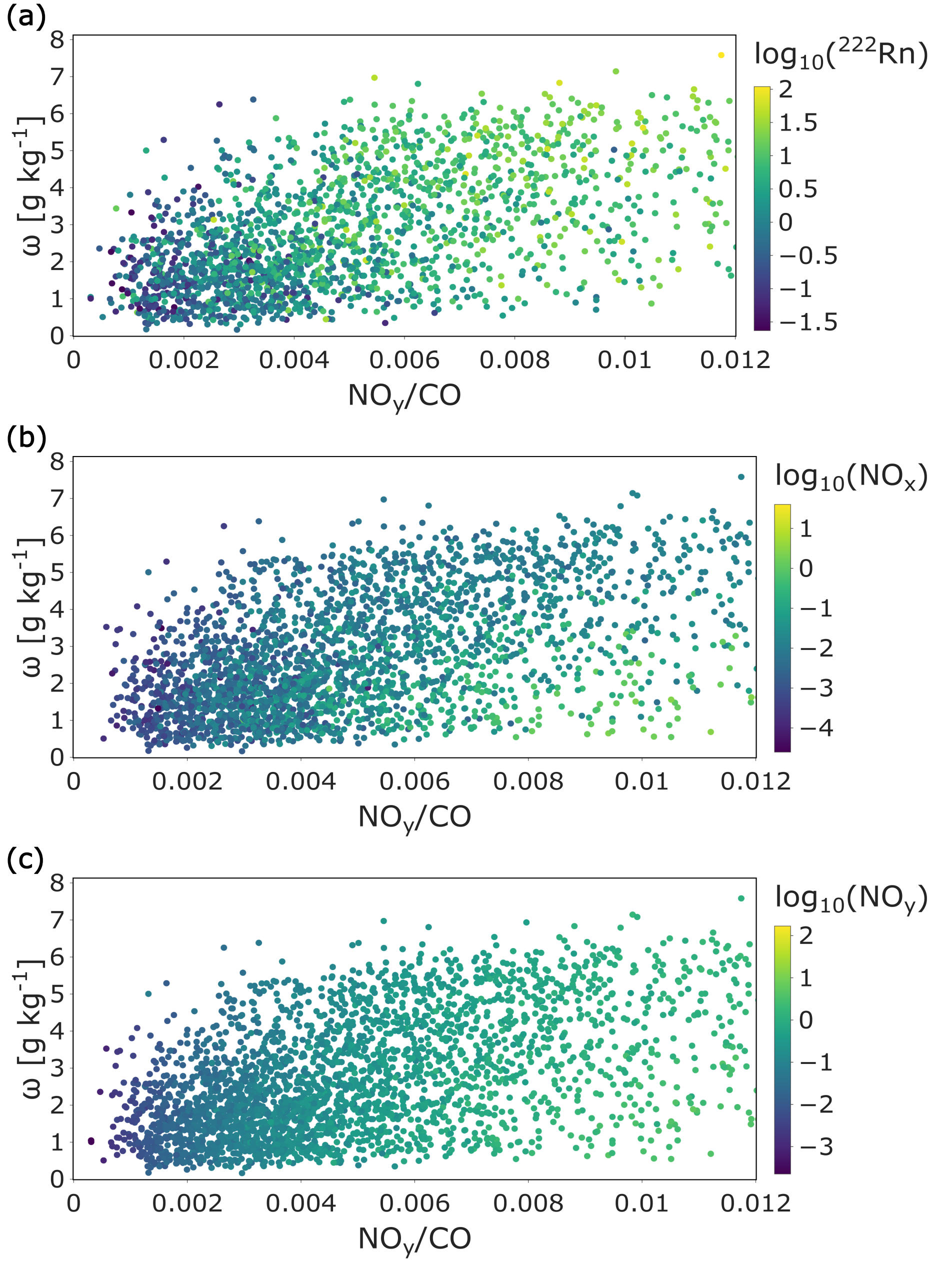

Figure S17. Comparison of ω and the PBLi tracer NO_y/CO, colored by the different gaseous and particle phase species: (a) decadic logarithm of ^{222}Rn concentrations $[\mathrm{Bq\,m^{-3}}]$, (b) decadic logarithm of NO_x mixing ratios $[\mathrm{ppb}]$ and (c) decadic logarithm of NO_y mixing ratios $[\mathrm{ppb}]$. Data points are daily averages from the periods of 2011 to 2012 and 2016 to 2019 for ^{222}Rn, and 2011 to 2019 for NO_x and NO_y. Data above $NO_y/CO = 0.012$ are not displayed for clarity of visualization (observations get sparse and trends are consistent).

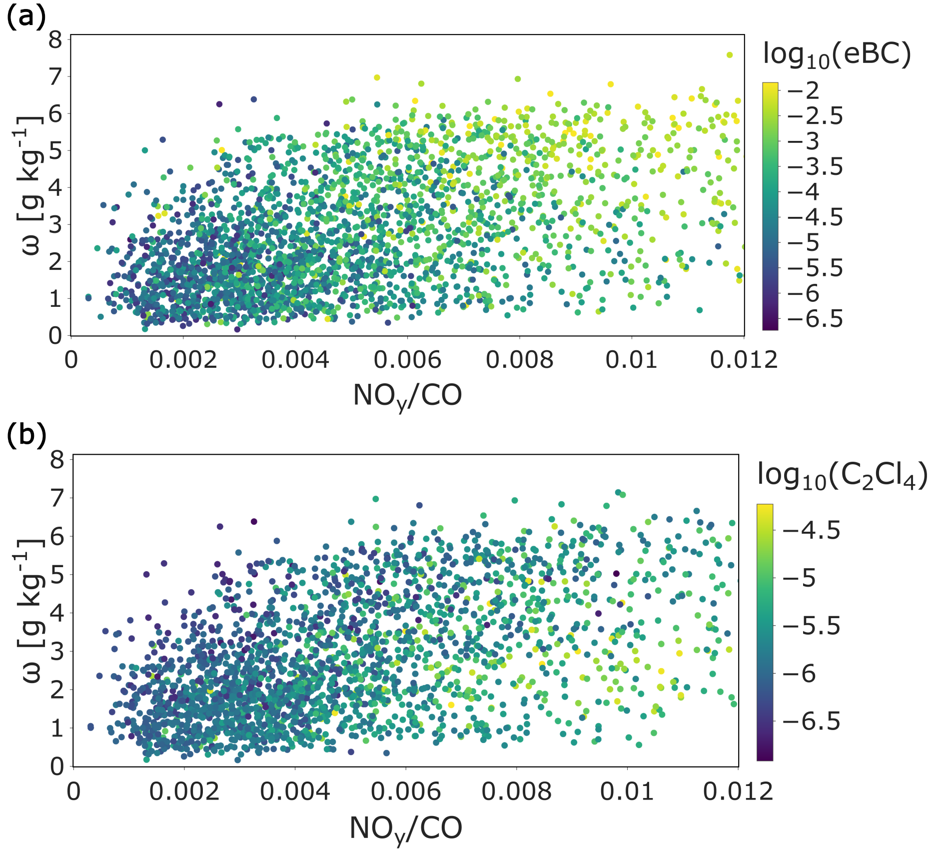

Figure S18. Just as Figure S17, but colored by (a) a decadic logarithm of eBC mass concentrations [$\mu g\,m^{-3}$] and (b) a decadic logarithm of tetrachloroethylene (C_2Cl_4) mixing ratios [ppb]. Data points are daily averages from the periods 2011 to 2019. Data above $NO_y/CO = 0.012$ are not displayed for clarity of visualization (observations get sparse and trends are consistent).

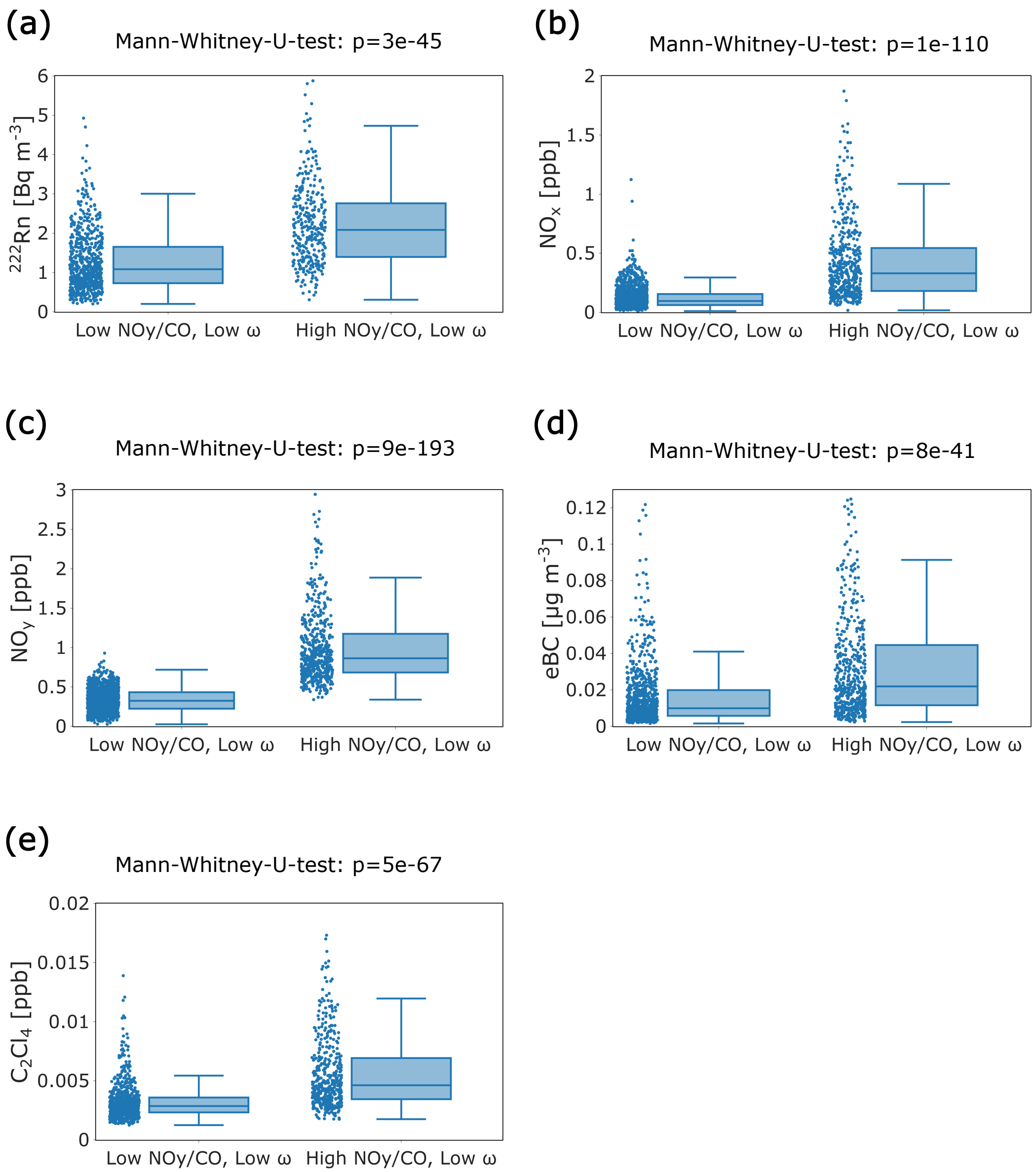

Figure S19. For the species displayed in Figure S17 and Figure S18, comparison of the low ω fractions (i.e. ≤ 3) for low NO_y/CO (≤ 0.005) and high NO_y/CO (≥ 0.005) in the form of box plots. Data were resampled for the two categories to have identical ω median values. Above each plot, the p-values of a Mann-Whitney-U-test are provided.

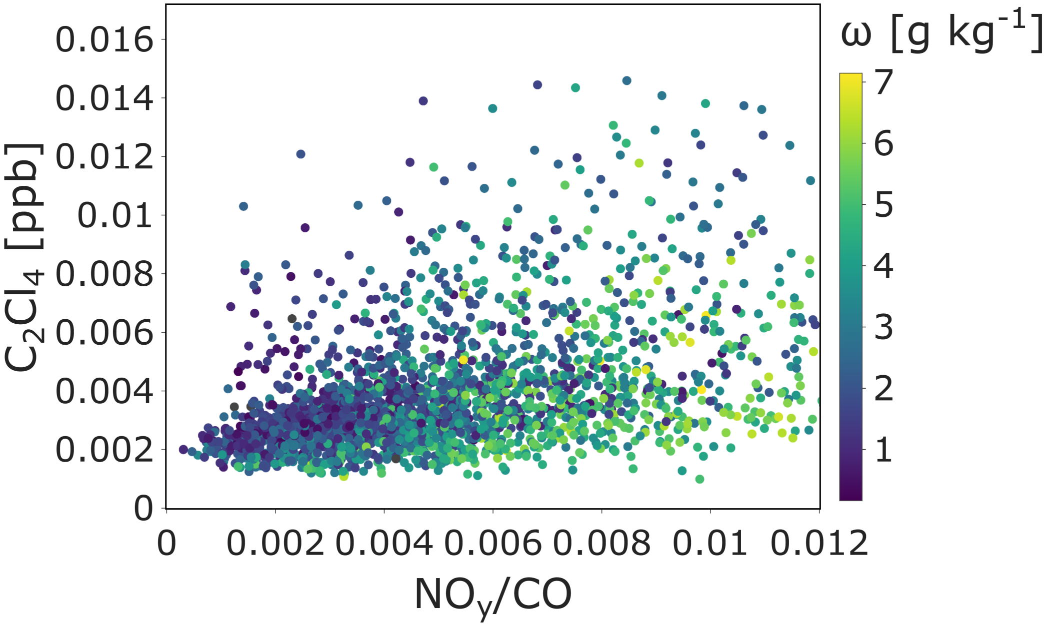

Figure S20. Tetrachloroethylene (C_2Cl_4) mixing ratios as a function of the PBLi tracer NO_y/CO, colored by ω. Data points are daily averages from the periods 2011 to 2019.

S9.3 Comparison of the different PBLi tracers and their dependence on ω

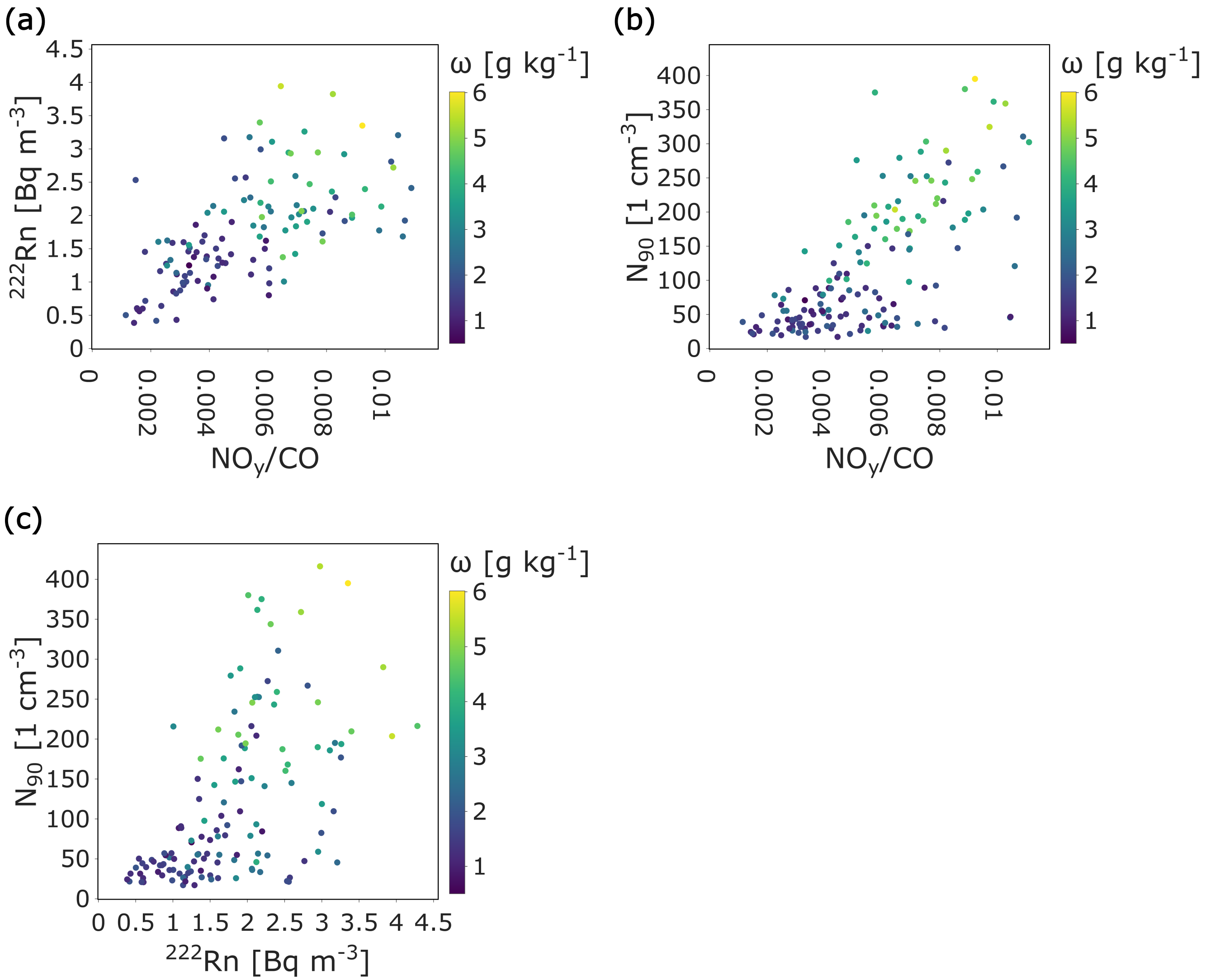

Figure S21. Comparison of different PBLi tracers, colored by ω. (a) ^{222}Rn as a function of NO_y/CO, (b) N_{90} as a function of NO_y/CO and (c) N_{90} as a function of ^{222}Rn. Depicted are averaged data for the same time periods as the composite samples chemically analyzed in this study. Sampling dates dominated by Saharan dust were omitted from all plots.

S10 Mass reconstruction of PM_{10} at the JFJ

S10.1 Fine-mode PM_1 aerosol

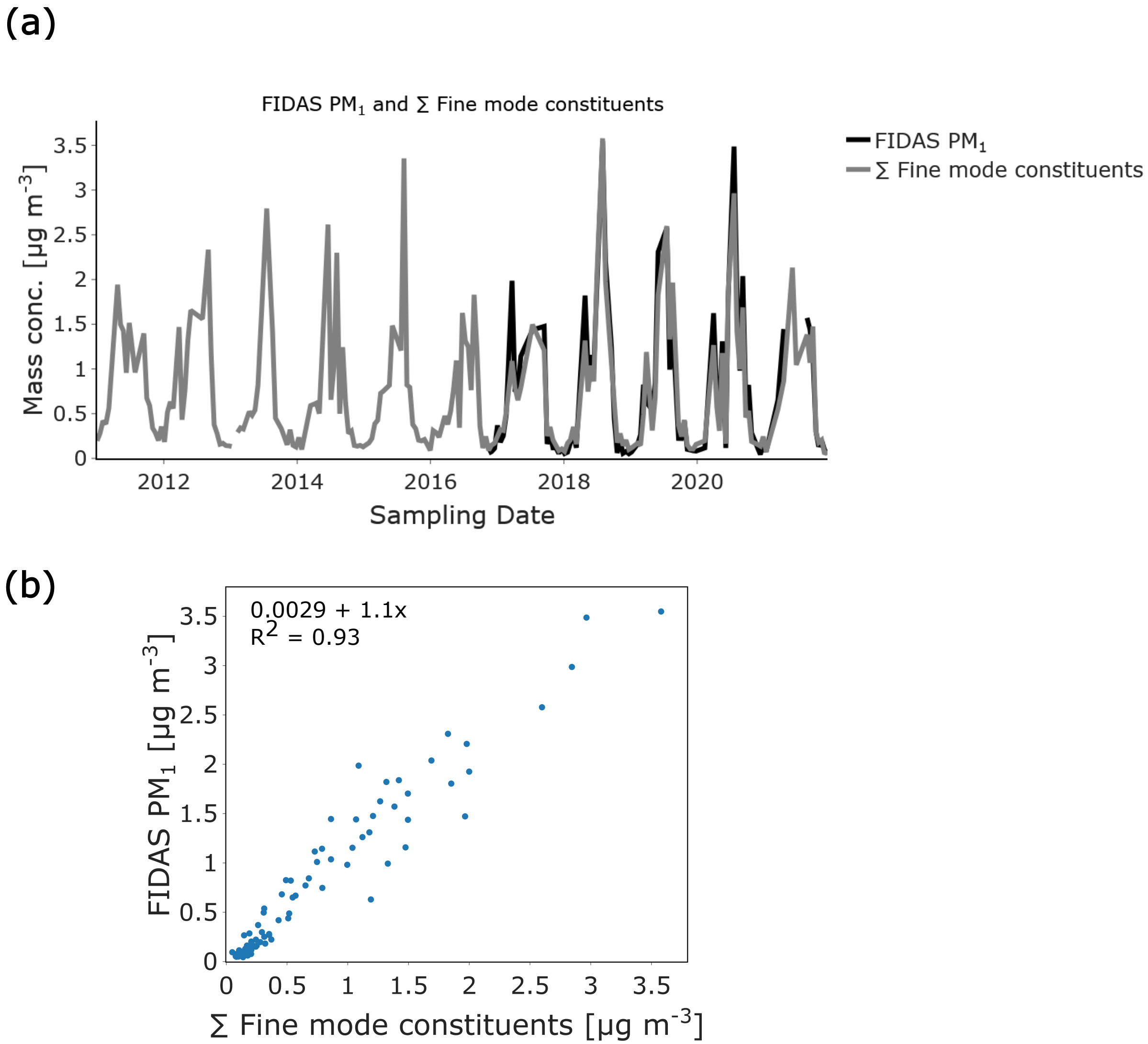

Figure S22. (a) Time series of FIDAS PM_1 (black, from October 2016) and a sum of the fine-mode aerosol constituent mass concentrations (grey) including WSOA, sulfate, and ammonium. (b) FIDAS PM_1 as a function of the mass concentrations of the summed constituents. A linear fit equation and coefficient of determination R^2 are provided.

S10.2 OC/EC ratios

For calculation of OC/EC ratios and display of seasonalities, only samples should be considered with EC concentrations above the limit of quantification of the SUNSET instrument. To assure this, samples were filtered based on a 3-sigma criterion with respect to fieldblank EC levels. For this, a threshold EC loading was calculated based on:

$$mean(fieldblanks)\ +\ 3 * \sigma(fieldlanks) \tag{S14}$$

with the mean and standard deviation of fieldblank loadings. Samples below that threshold were not considered in the calculation.

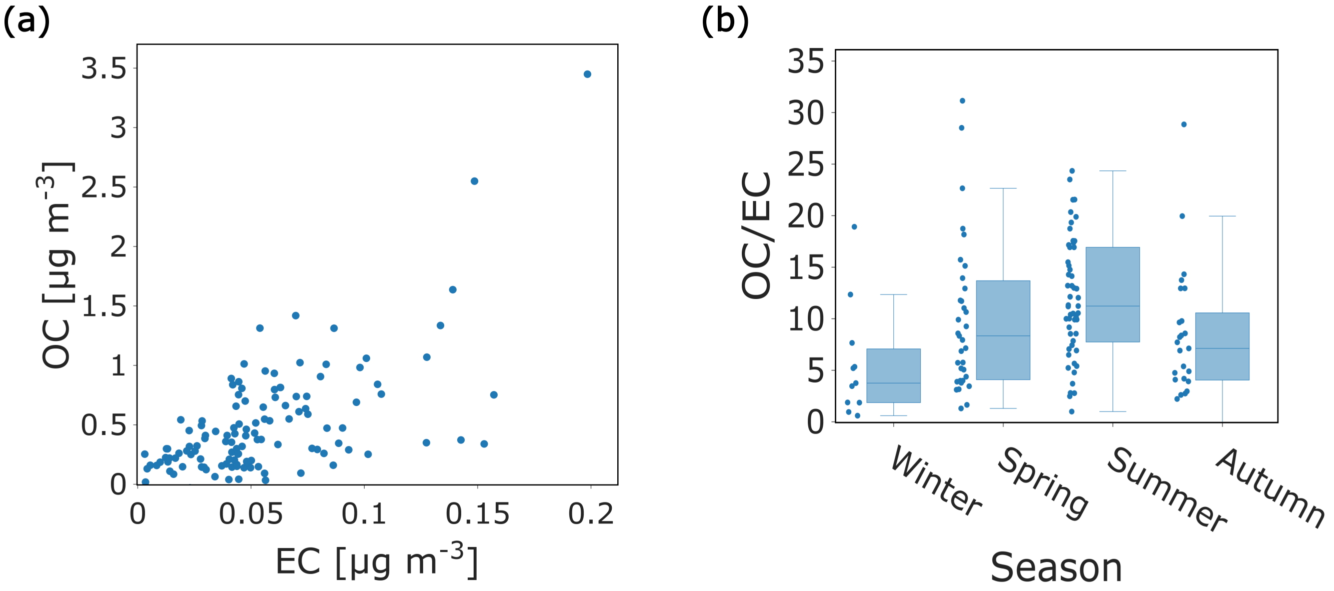

Figure S23. (a) Comparison of OC and EC ambient concentrations at the JFJ and (b) seasonal OC/EC ratios. Data are filtered based on a 3 sigma criterion for sample filter EC loadings above fieldblank levels. Data is from the periods of August 2013 to September 2014 and March 2019 to November 2019 (daily filter samples).

S10.3 WSOC/OC ratios as an indicator for water solubility of OA at the JFJ

WSOC/OC can be seen as a good indicator for water solubility of OA. For a quantitative assessment based on OA mass, the differences in OM/OC ratios between WSOA and OA would also have to be taken into account. As the water-insoluble part of OA can be expected to have lower OM/OC due its lower polarity (and therefore less relative amount of heteroatoms that contribute to OM), the actual water solubility of OA lies above the $83\,\%$ estimated from a linear fit of OC vs. WSOC (Figure S24).

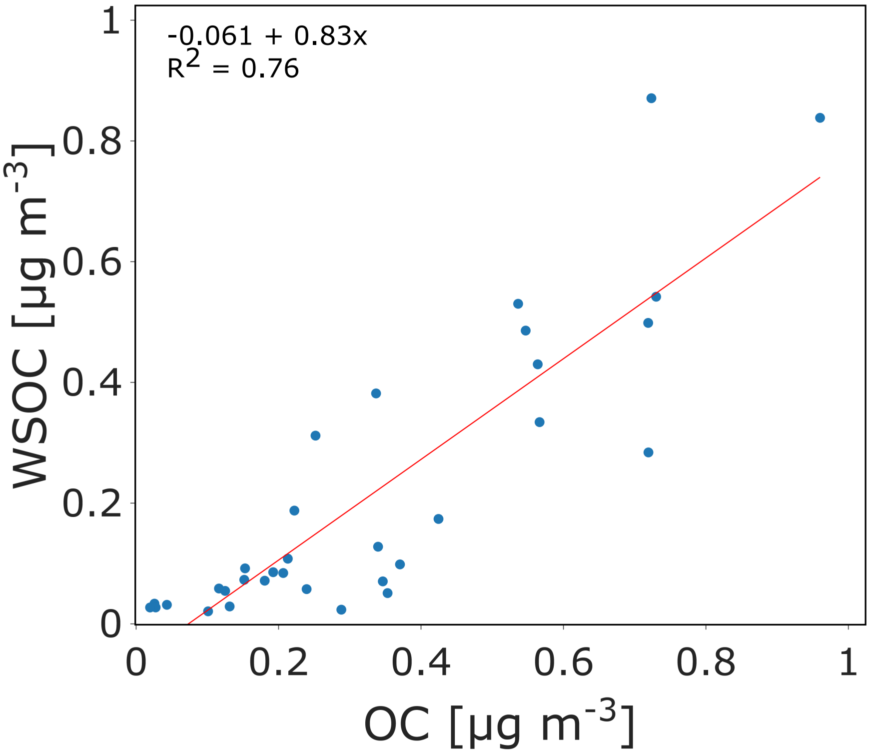

Figure S24. Comparison of OC and WSOC ambient concentrations at the JFJ. WSOC was obtained from the Offline-AMS quantified WSOA by division with Offline-AMS OM/OC-ratios. Data is from the periods of August 2013 to September 2014 and March 2019 to November 2019 (composite filter samples). In the scatter plot, a linear fit is plotted and the fit equation and coefficient of determination R^2 are provided.

S10.4 Coarse-mode PM_{1-10} aerosol

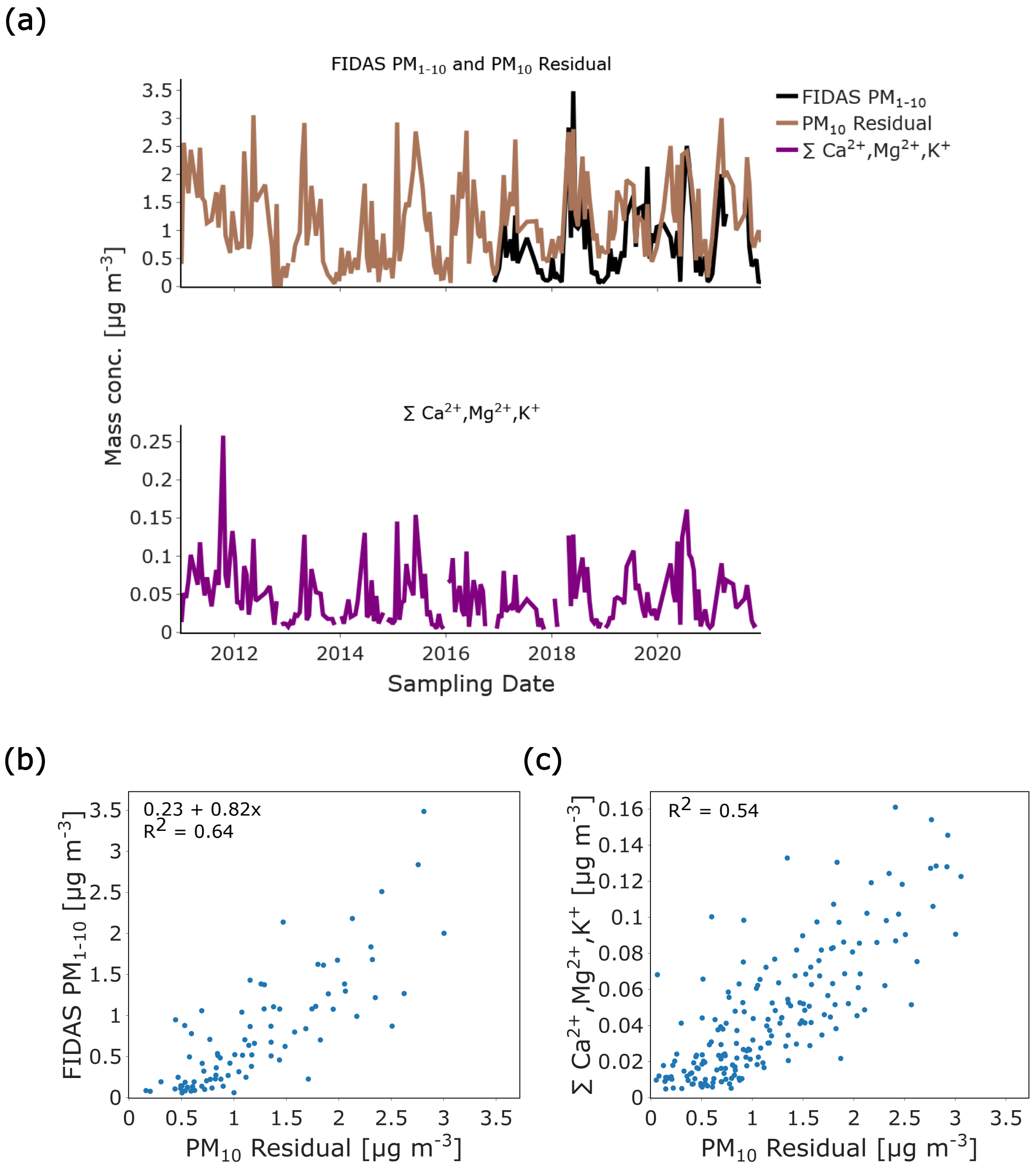

Figure S25. (a) Mass concentration time series of FIDAS PM_{1-10} (black, from October 2016), the residual of gravimetric PM_{10} after subtraction of WSOA, sulfate and ammonium (beige) and the sum of the ions Ca^{2+}, Mg^{2+} and K^{+} (purple). Gravimetric PM_{10} residual as a function of (b) FIDAS PM_{1-10} and (c) the sum of Ca^{2+}, Mg^{2+} and K^{+}. A linear fit equation and coefficients of determination R^2 are provided.

S10.5 Mass reconstruction of mineral dust and comparison with coarse-mode aerosol loadings

Mass reconstruction of mineral dust was carried out based on ICP-MS elemental data, following an approach described by Hueglin et al. (2005). The major elements by abundance Al, Mg, K, Ca and Fe were considered as well as an estimated concentration of Si (which cannot be quantified from quartz filter samples). For estimating Si, the average ratio of Si and Al in the earth's crust was applied: $Si = 3.41Al$. Under the assumption that elements are present in form of their oxides, mineral dust mass was calculated from element concentrations (mild mineralization recovery corrected, cf. subsection S2.3) using the factors: $1.89Al + 1.66Mg + 1.21K + 1.40Ca + 1.43Fe + 2.14Si$ (Hueglin et al., 2005; Chow et al., 1994). For a more complete reconstruction of coarse-mode mass, the sum of trace element concentrations was also calculated (including Li, Be, B, Na, Sc, Ti, V, Cr, Mn, Co, Ni, Cu, Zn, Ga, Ge, As, Rb, Sr, Y, Zr, Mo, Cd, Sn, Sb, Cs, Ba, La, Ce, Sm, Tb, Pb, Th, U).

The very low ambient aerosol concentrations at the JFJ (especially under FT-like conditions) and the necessity of applying a mild mineralization of filter material to minimize matrix effects (cf. subsection S2.3) led to only a small fraction of samples showing all major elements above limits of quantification (overall 21 samples). Only these samples were considered for reconstruction of relative elemental composition and comparison to coarse-mode levels. In light of this, the aim of the mineral dust mass reconstruction done here is primarily to provide a good estimate of coarse-mode composition at the JFJ (in the absence of Saharan dust) and not to quantitatively describe composition seasonal variability.

In Figure S26, the recovery ratio of coarse-mode aerosol by mineral dust and trace element mass concentrations is shown in the form of a box plot. It is calculated in the following way (with *conc.*: mass concentrations):

$$coarse\ mode\ recovery\ ratio = \frac{conc.(mineral\ dust\ +\ trace\ elements)}{PM_{10}(gravimetric) - conc.(WSOA\ +\ sulfate\ +\ ammonium)} \tag{S15}$$

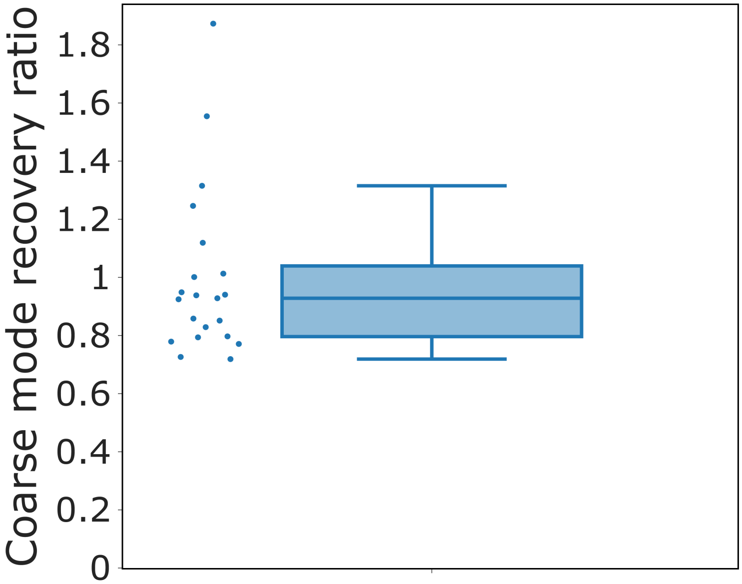

Figure S26. Box plot of the coarse-mode recovery ratio, i.e. the ratio of the reconstructed mass of mineral dust and trace elements (from ICP-MS data) and the gravimetric PM_{10} fraction after subtraction of fine-mode constituents (WSOA, sulfate and ammonium). Only samples with a full set of major mineral dust elements (Al, Mg, K, Ca, Fe, estimated Si) above limits of detection were considered. Sampling dates dominated by Saharan dust were not considered.

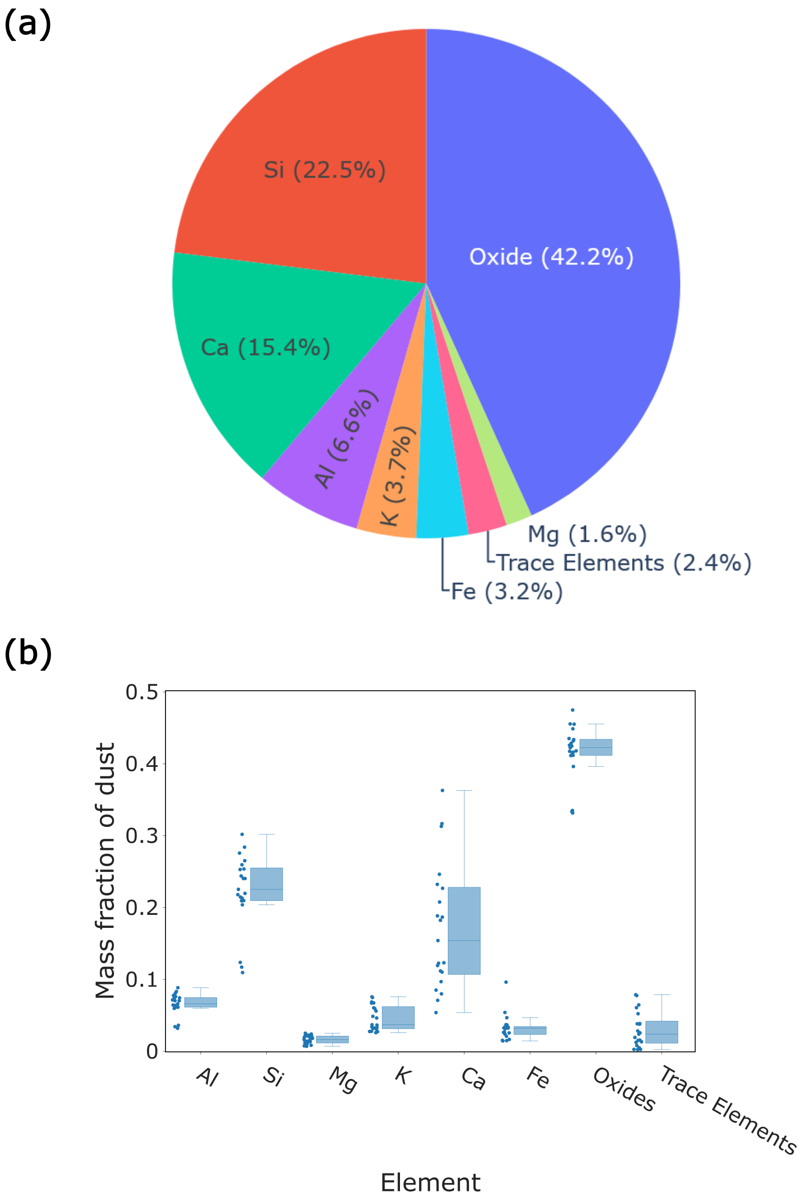

Figure S27. Elemental composition of the coarse-mode aerosol fraction at the JFJ (long-range transported Saharan dust dominated conditions excluded), composed of mineral dust and trace elements in the form of (a) a pie chart of median values and (b) a box plot showing the mass fraction of each element to total mass of mineral dust and trace elements. Only samples with a full set of major mineral dust elements (Al, Mg, K, Ca, Fe, estimated Si) above limits of detection were considered. All major elements are assumed to be present in the form of their oxides.

S10.6 Mass concentration seasonalities of selected $PM10$ constituents and $PM10$ fractions

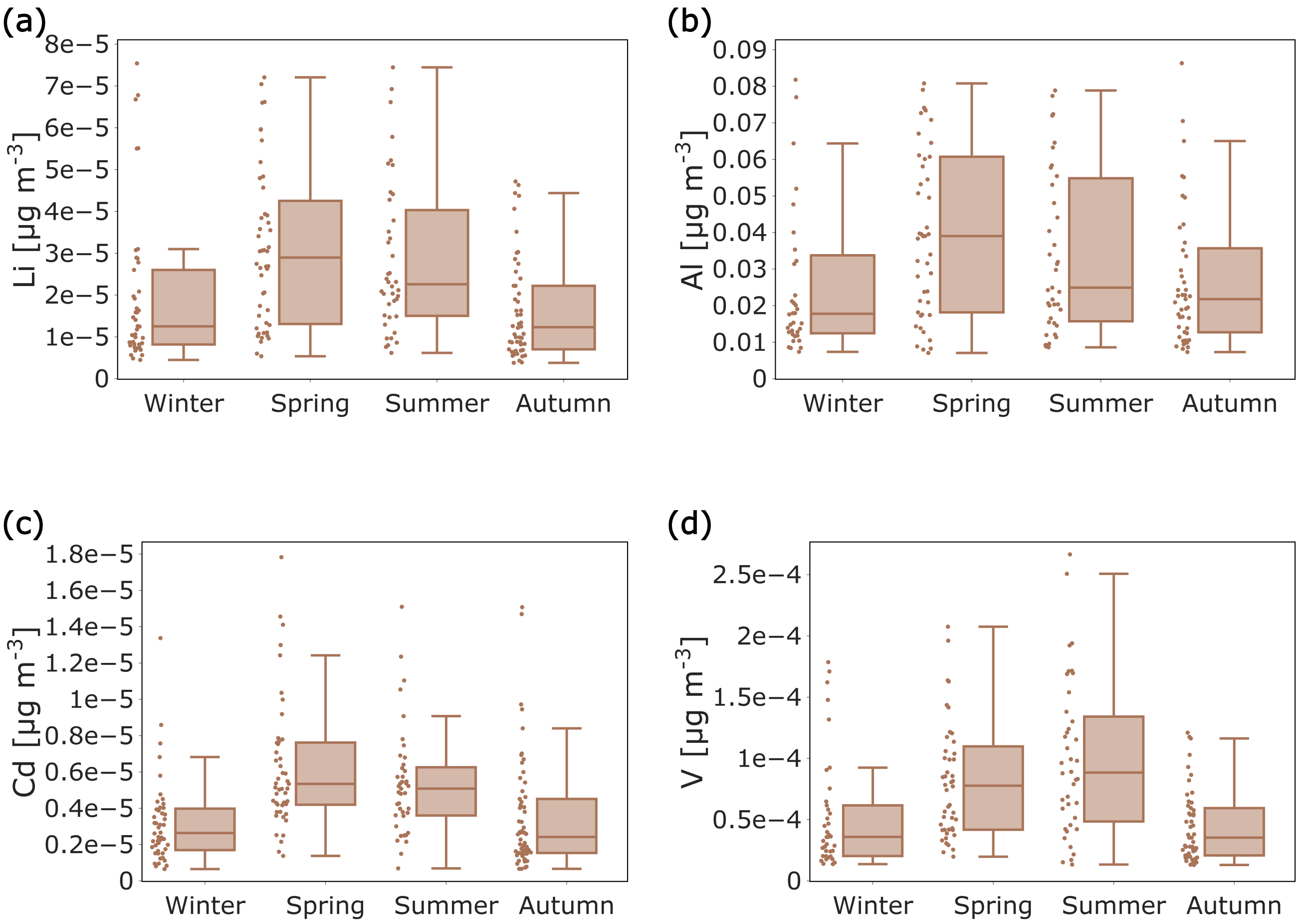

Figure S28. Seasonal trends of mass concentrations for the typical coarse-mode metal aerosol constituents (a) lithium and (b) aluminum, as well as typical fine-mode constituents (c) cadmium and (d) vanadium at the JFJ. All data are from ICP-MS. Seasons are defined as Winter - DJF, Spring - MAM, Summer - JJA, Autumn - SON. Sampling dates dominated by Saharan dust were not considered.

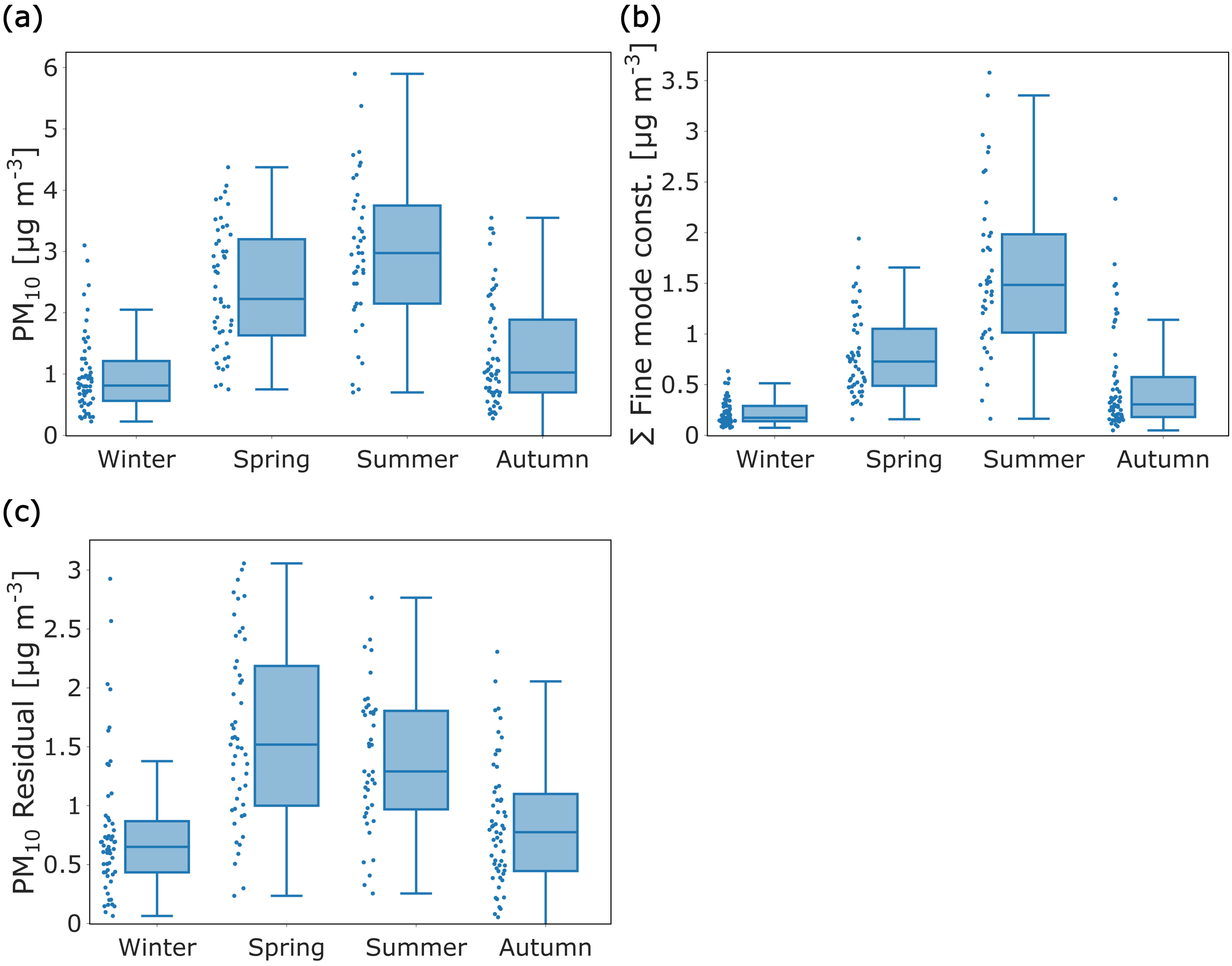

Figure S29. Seasonal trends of different bulk aerosol mass concentrations at the JFJ: (a) Gravimetric PM_{10}, (b) fine-mode aerosol (PM_1) as represented by the sum of the fine-mode aerosol constituent WSOA, sulfate and ammonium, (c) coarse-mode aerosol (PM_{1-10}) as represented by the residual of gravimetric PM_{10} after subtraction of WSOA, sulfate and ammonium. Seasons are defined as Winter - DJF, Spring - MAM, Summer - JJA, Autumn - SON. Sampling dates dominated by Saharan dust were not considered.

S11 The dependence of VOC mixing ratios on NO_y/CO and ω at the JFJ

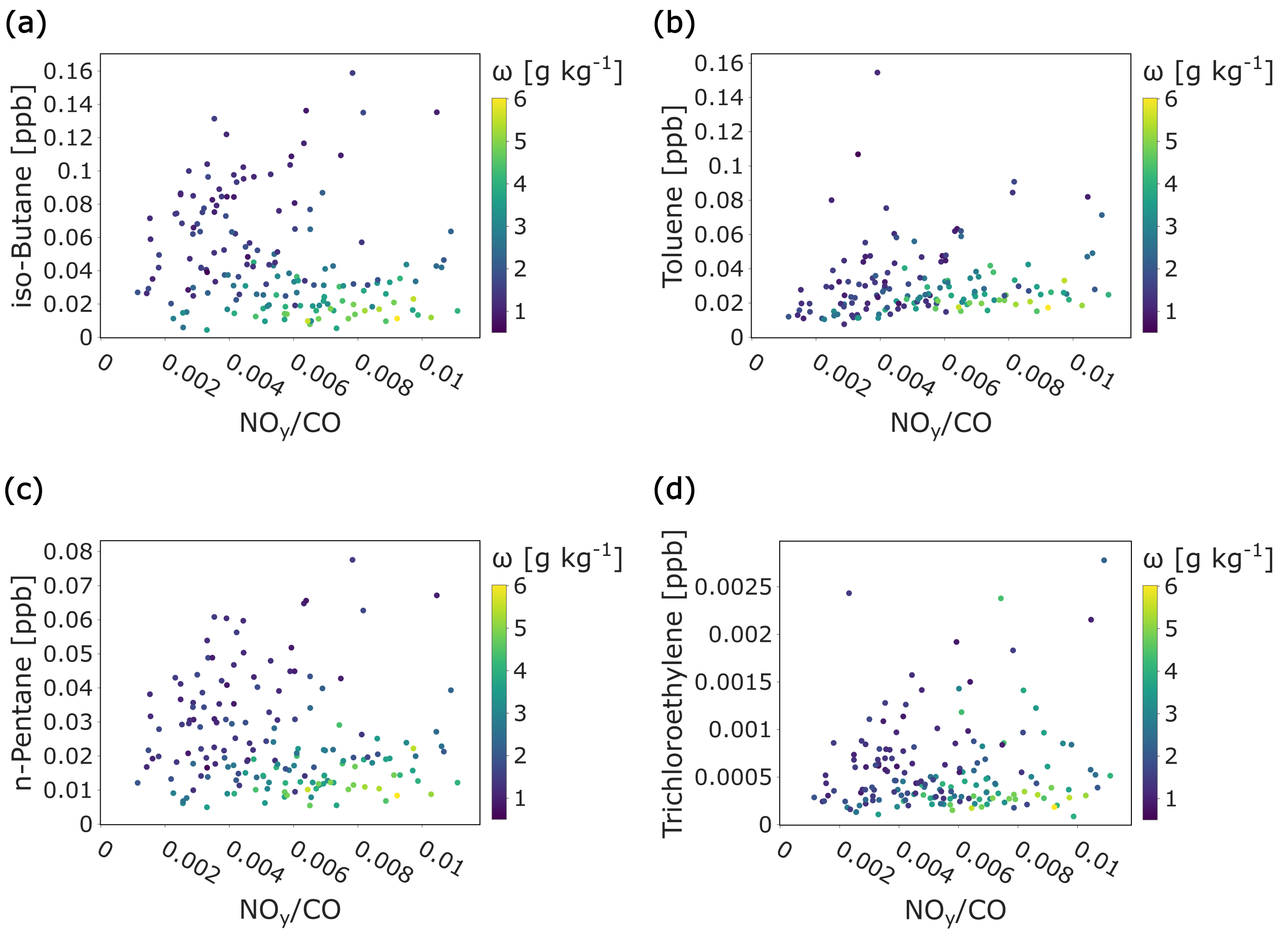

Figure S30. Mixing ratios of (a) *iso*-Butane, (b) toluene, (c) *n*-Pentane and (d) trichloroethylene as a function of NO_y/CO at the JFJ, colored by ω. Depicted are average data for the same time periods as the composite samples chemically analyzed in this study (data from 2011 to 2020).

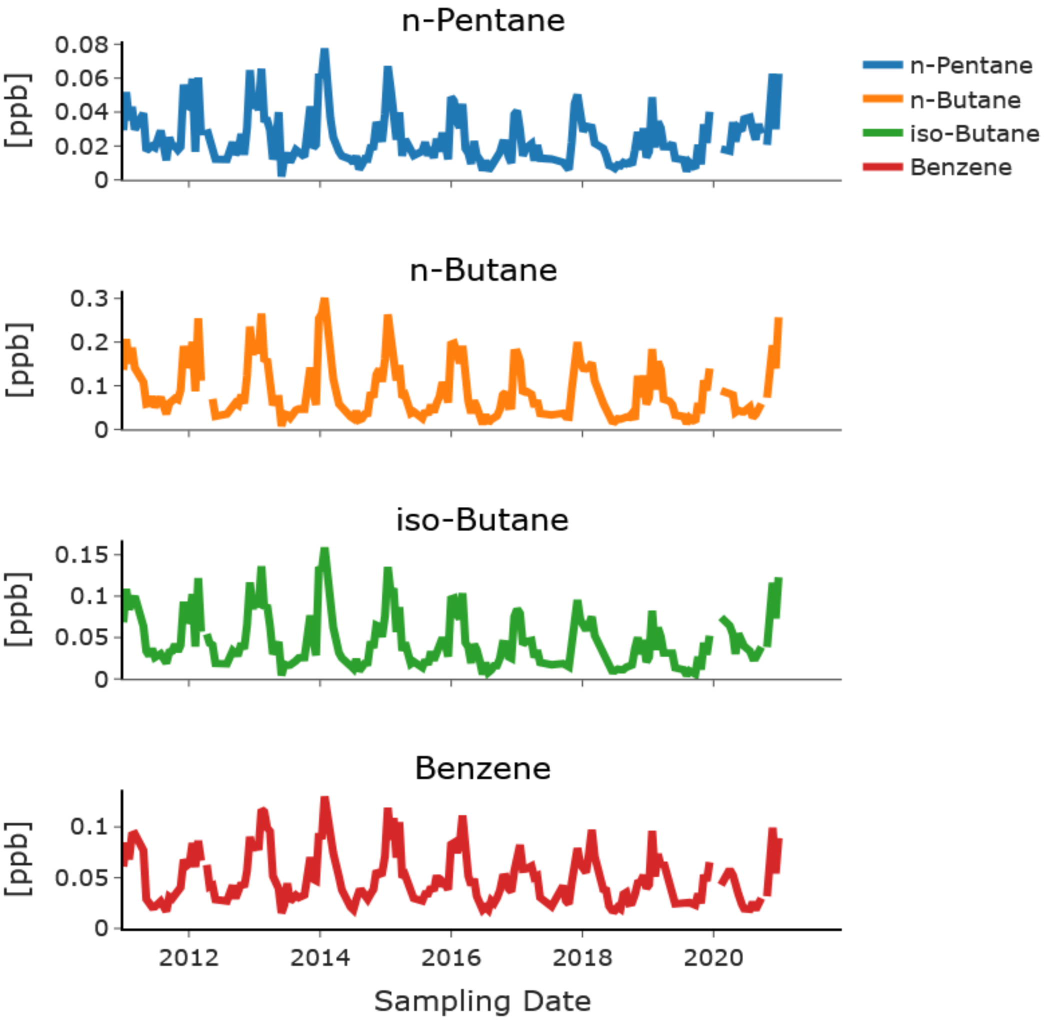

Figure S31. Mixing ratio time series of the NMHCs *n*-Pentane, *n*-Butane, *iso*-Butane and Benzene from 2011 to 2020 at the JFJ.

S12 Behavior of PM_1 and eBC with respect to NO_y/CO and ω

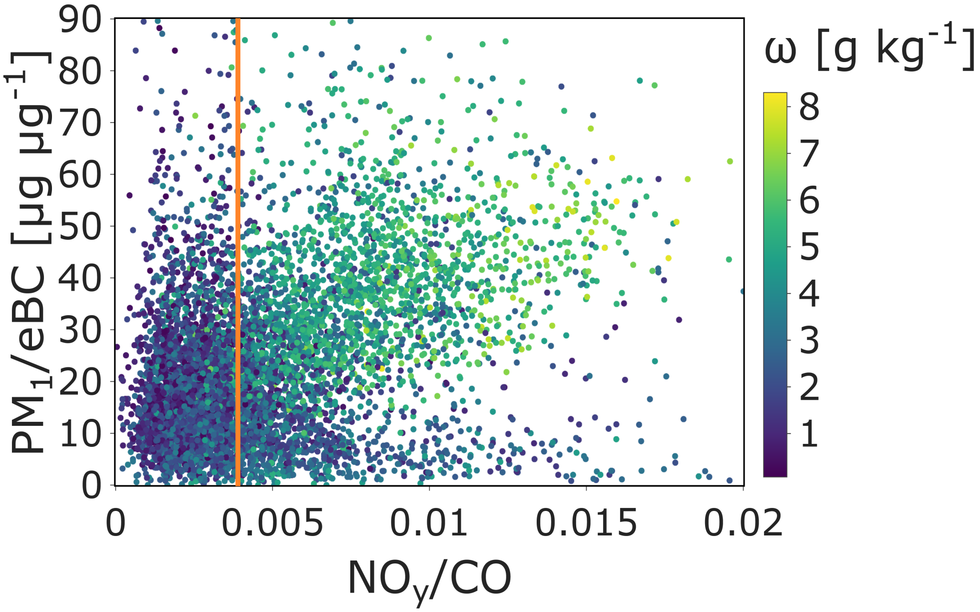

Figure S32. The ratio of PM_1/eBC at the JFJ as a function of the PBLi tracer NO_y/CO, colored by ω. The orange vertical line indicates the threshold $NO_y/CO = 0.004$ used in Figure 5 of the main manuscript. PM_1 data is from online FIDAS measurements. Data points are $3\,\mathrm{h}$ aggregated averages of the whole period between November 2016 and February 2020. Sampling dates dominated by Saharan dust were omitted based on high-time-resolution optical flags.

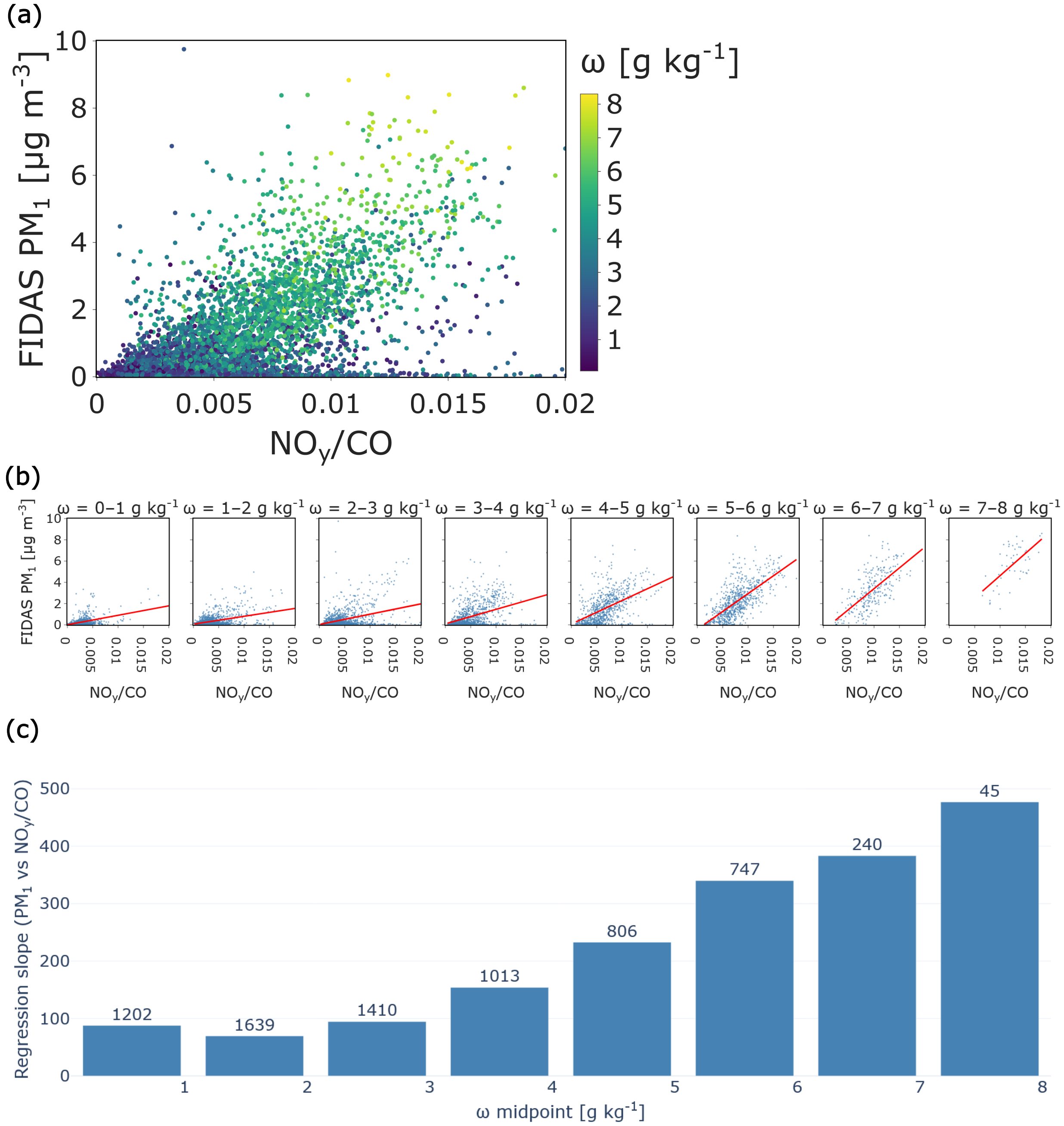

Figure S33. (a) FIDAS PM_1 as a function of the PBLi transport tracer NO_y/CO, colored by ω. (b) The analogous plots of FIDAS PM_1 as a function of NO_y/CO, binned for different levels of ω (as indicated above each sub-plot). (c) Linear regression slopes for the plots displayed in (b), with the number of data points considered for each regression denoted above each bar. A higher slope represents a stronger increase with NO_y/CO at a certain level of ω. Data points are 3 h averages of the whole period between November 2016 and February 2020. Sampling dates dominated by Saharan dust were omitted based on high-time-resolution optical flags.

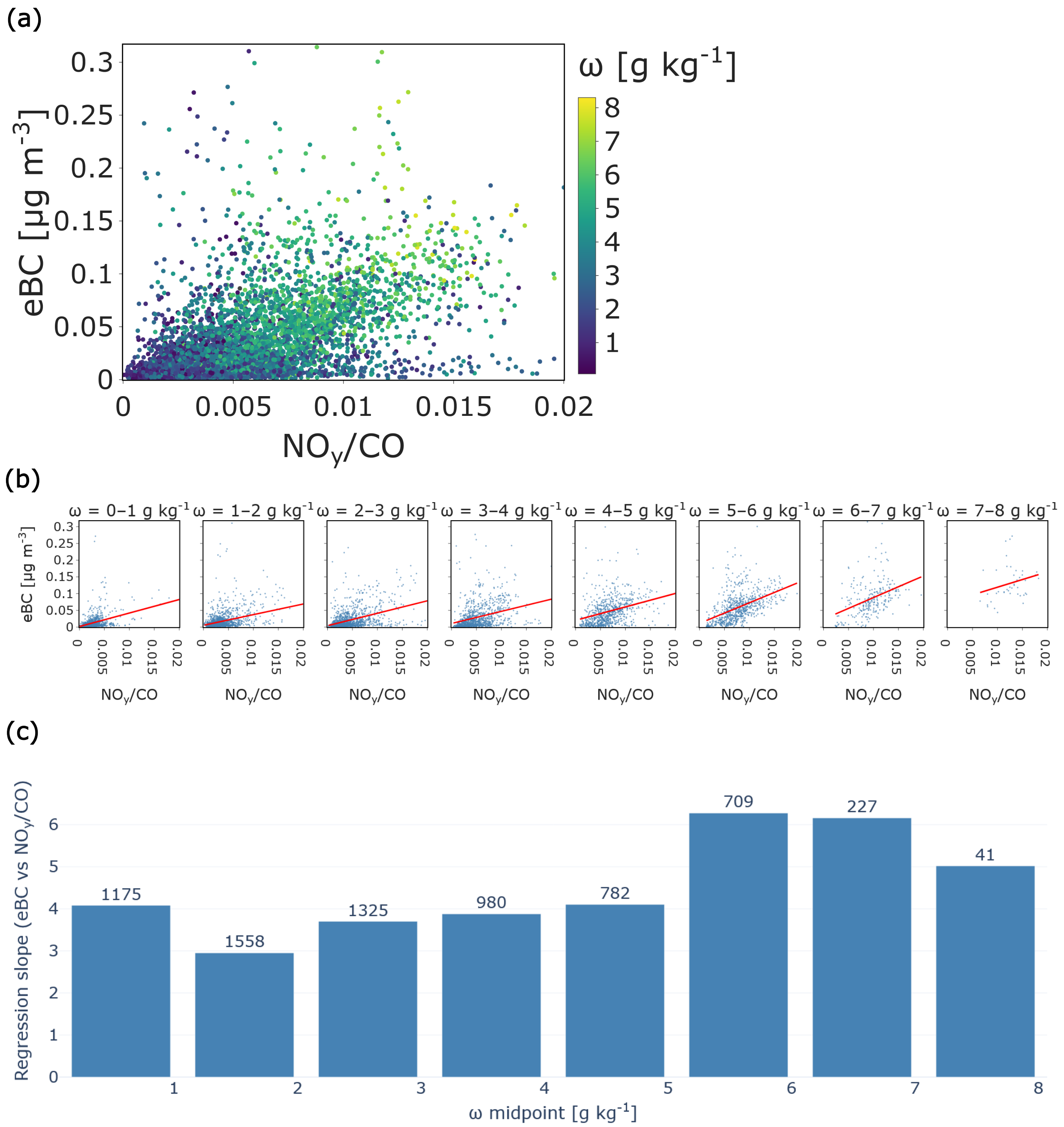

Figure S34. (a) eBC as a function of the PBLi transport tracer NO_y/CO, colored by ω. (b) The analogous plots of eBC as a function of NO_y/CO, binned for different levels of ω (as indicated above each sub-plot). (c) Linear regression slopes for the plots displayed in (b), with the number of data points considered for each regression denoted above each bar. A higher slope represents a stronger increase with NO_y/CO at a certain level of ω. Data points are 3 h averages of the whole period between November 2016 and February 2020. Sampling dates dominated by Saharan dust were omitted based on high-time-resolution optical flags.

S13 Dependence of aerosol constituent mass concentrations on NO_y/CO and ω

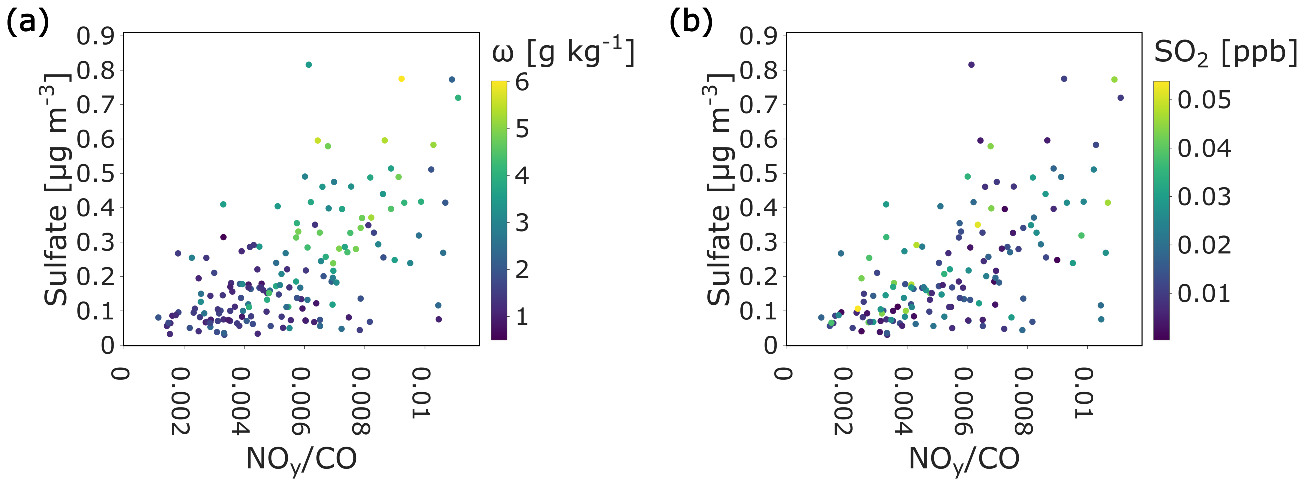

Figure S35. Sulfate ambient concentrations at the JFJ as a function of the PBLi tracer NO_y/CO, colored by (a) ω and (b) SO_2. Sulfate data is from IC-MS, SO_2 from online *in-situ* measurements.

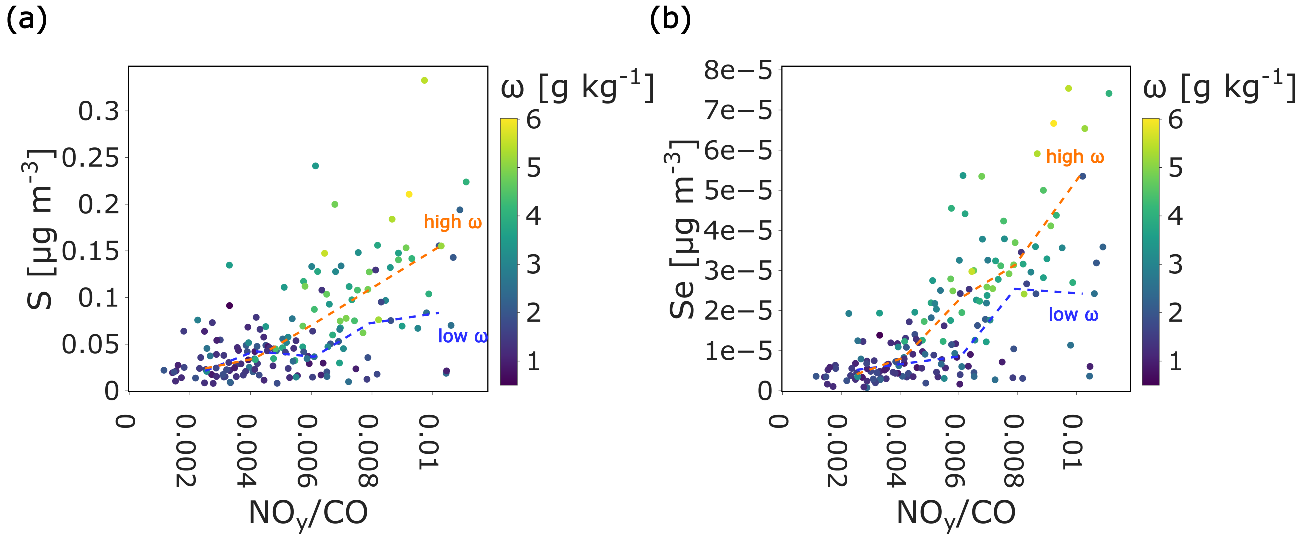

Figure S36. (a) Elemental sulfur and (b) selenium ambient concentrations at the JFJ as a function of the PBLi tracer NO_y/CO, colored by ω. Data is from ICP-MS. Binned local median trend lines of mass concentrations vs. NO_y/CO for low (blue) and high (orange) ω are displayed. For this, data were stratified into five discrete NO_y/CO bins, locally segregated by upper/lower half of ω observations and the medians for the low and high ω groups were calculated to obtain trend lines. Sampling dates dominated by Saharan dust were omitted from all plots.

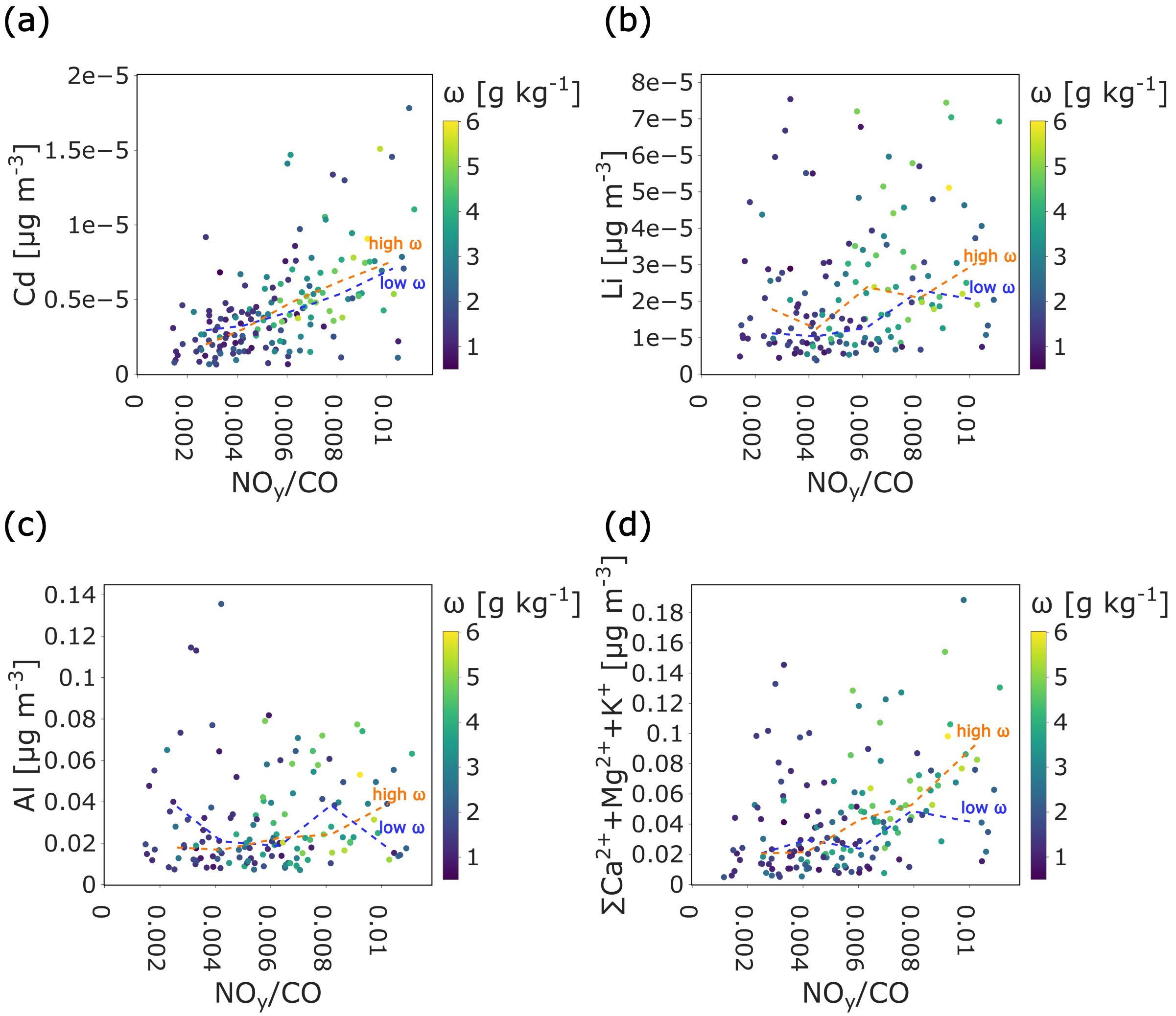

Figure S37. (a) Cadmium, (b) lithium, (c) aluminum and (d) the sum of Ca^{2+}, Mg^{2+} and K^{+} ions ambient concentrations at the JFJ as a function of the PBLi tracer NO_y/CO, colored by ω. Data is from ICP-MS and IC-MS. Binned local median trend lines of mass concentrations vs. NO_y/CO for low (blue) and high (orange) ω are displayed. For this, data were stratified into five discrete NO_y/CO bins, locally segregated by upper/lower half of ω observations and the medians for the low and high ω groups were calculated to obtain trend lines. Sampling dates dominated by Saharan dust were omitted from all plots.

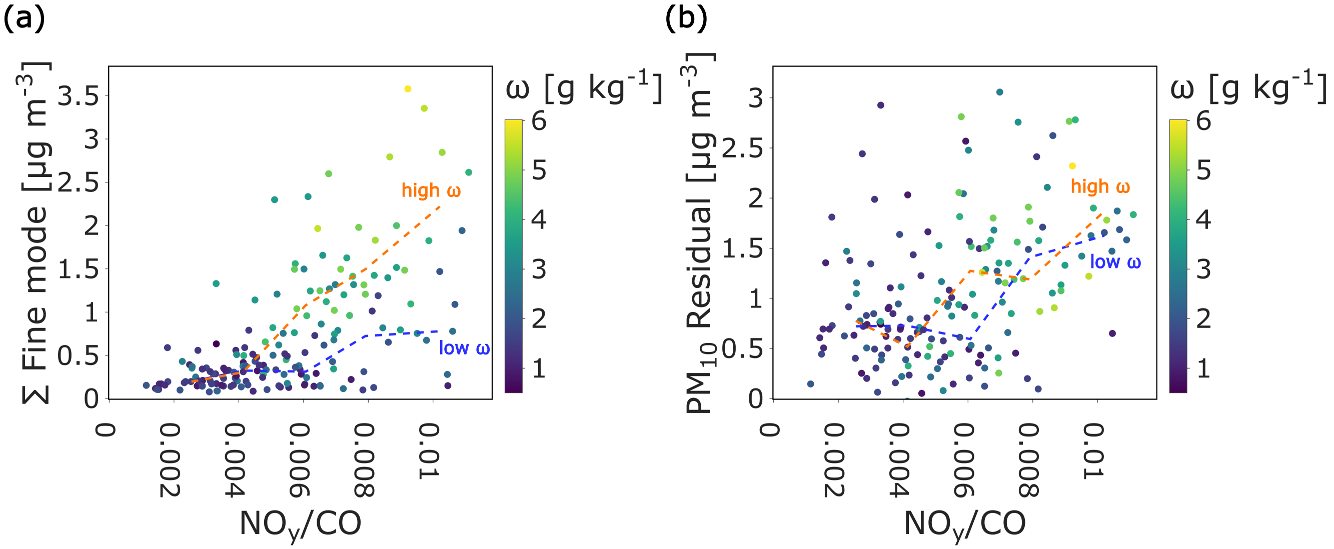

Figure S38. (a) Fine-mode fraction and (b) PM_{10} Residual of the aerosol at the JFJ as a function of the PBLi tracer NO_y/CO, colored by ω. Fine-mode is calculated as the sum of WSOA, sulfate and ammonium. PM_{10} Residual is calculated by subtracting fine-mode constituents from PM_{10}. Binned local median trend lines of mass concentrations vs. NO_y/CO for low (blue) and high (orange) ω are displayed. For this, data were stratified into five discrete NO_y/CO bins, locally segregated by upper/lower half of ω observations and the medians for the low and high ω groups were calculated to obtain trend lines. Sampling dates dominated by Saharan dust were omitted from all plots.

S14 Molecular secondary organic aerosol marker reactivity in the light of atmospheric oxidative capacity

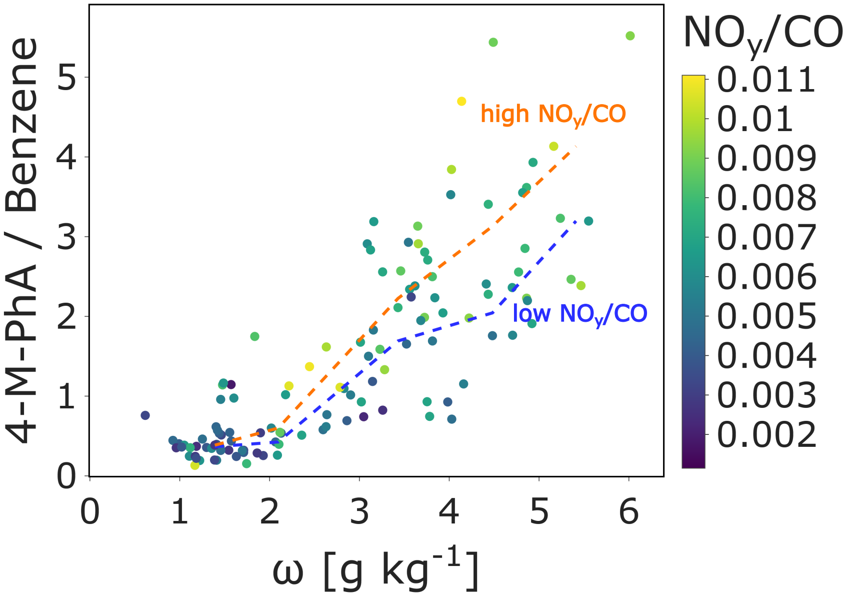

Figure S39. Ratio of 4-methylphthalic acid (4-M-PhA) mass concentrations $[\mathrm{ng\,m^{-3}}]$ and benzene mixing ratio $[\mathrm{ppb}]$ at the JFJ as a function of ω, colored by the PBLi tracer NO_y/CO. Binned local median trend lines of the ratio vs. ω for low (blue) and high (orange) NO_y/CO are displayed. For this, data were stratified into six discrete ω bins, locally segregated by upper/lower half of NO_y/CO observations and the medians for the low and high NO_y/CO groups were calculated to obtain trend lines. Sampling dates dominated by Saharan dust were omitted from the plot.

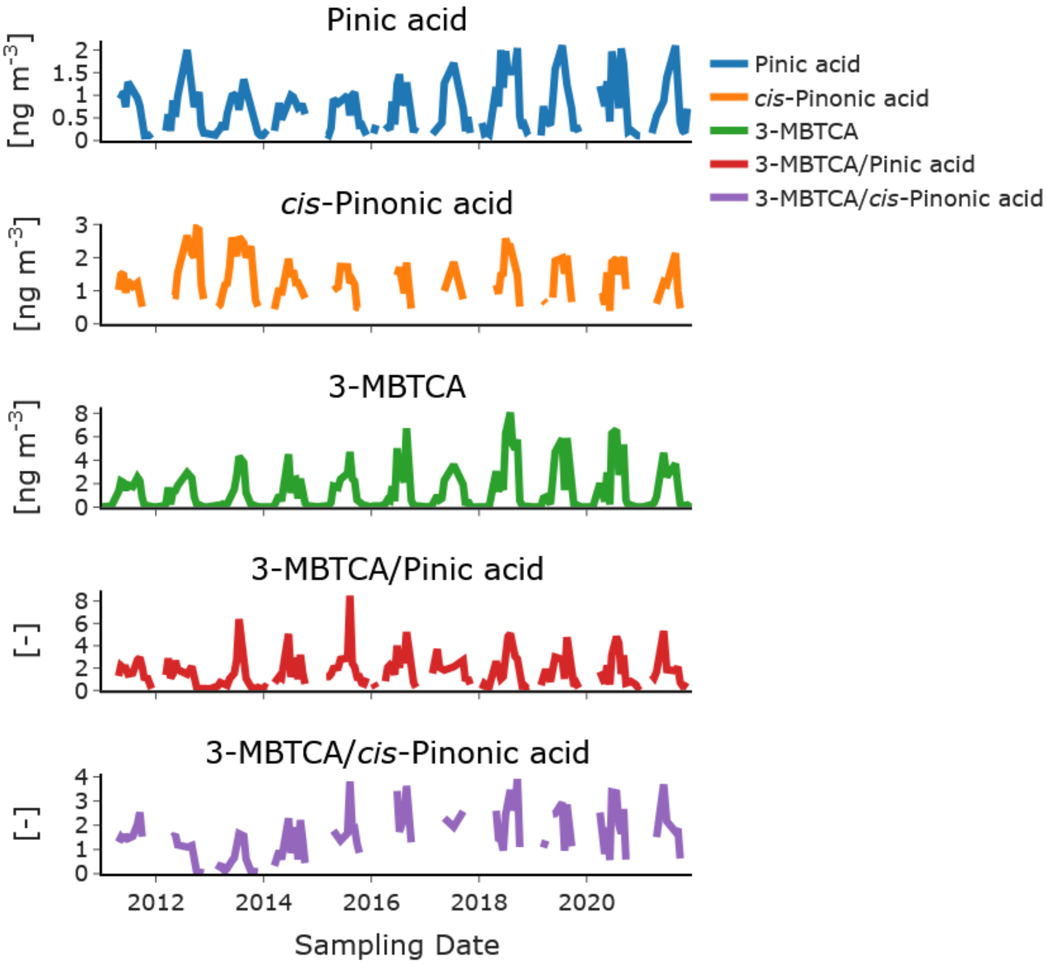

Figure S40. Time series of mass concentrations for the three α-pinene derived SOA markers pinic acid, *cis*-pinonic acid and 3-methylbutane-1,2,3-tricarboxylic acid (3-MBTCA) at the JFJ and the respective ratios 3-MBTCA/pinic acid and 3-MBTCA/*cis*-pinonic acid. Missing data points are due to sample concentrations below limit of quantification.

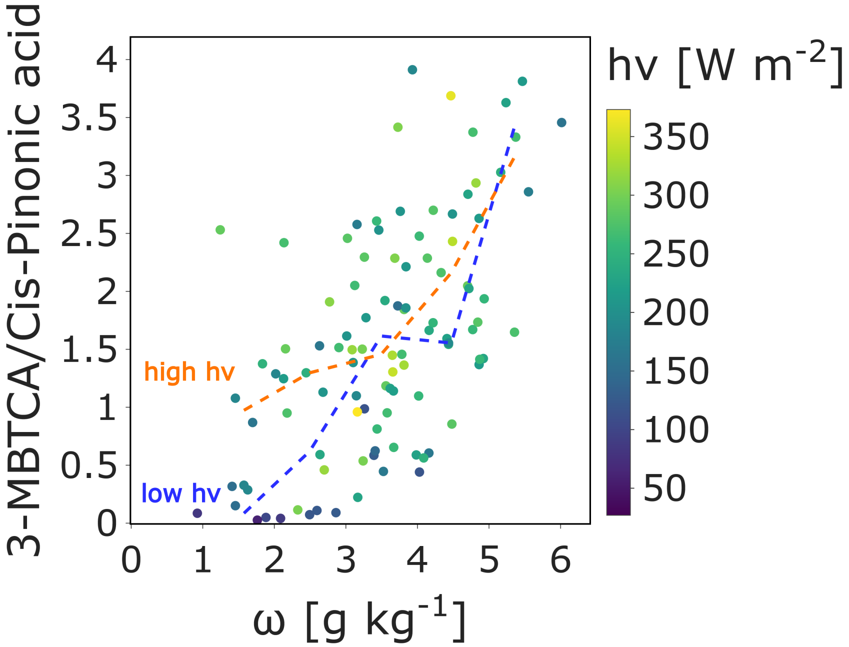

Figure S41. Mass concentration [$\mathrm{ng\,m^{-3}}$] ratio of the biogenic SOA markers 3-MBTCA and *cis*-pinonic acid at the JFJ as a function of ω, colored by global radiation intensity ($h\nu$). Binned local median trend lines of the ratio vs. ω for low (blue) and high (orange) $h\nu$ are displayed. For this, data were stratified into six discrete ω bins, locally segregated by upper/lower half of $h\nu$ observations and the medians for the low and high $h\nu$ groups were calculated to obtain trend lines. Sampling dates dominated by Saharan dust were omitted from the plot.

S15 WSOA chemical composition in the light of NO_y/CO and ω

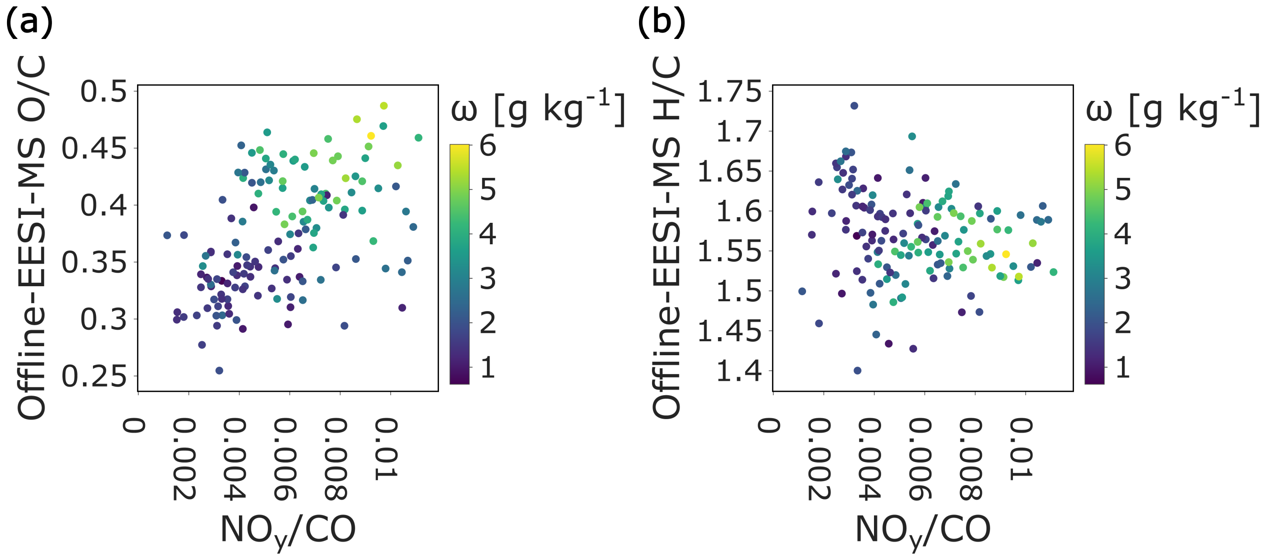

Figure S42. Offline-EESI-MS atomic (a) O/C- and (b) H/C-ratios of the WSOA at JFJ as a function of the PBLi tracer NO_y/CO, colored by ω. Sampling dates dominated by Saharan dust were omitted from the plot. Data is from composite filter samples from 2011 to 2019.

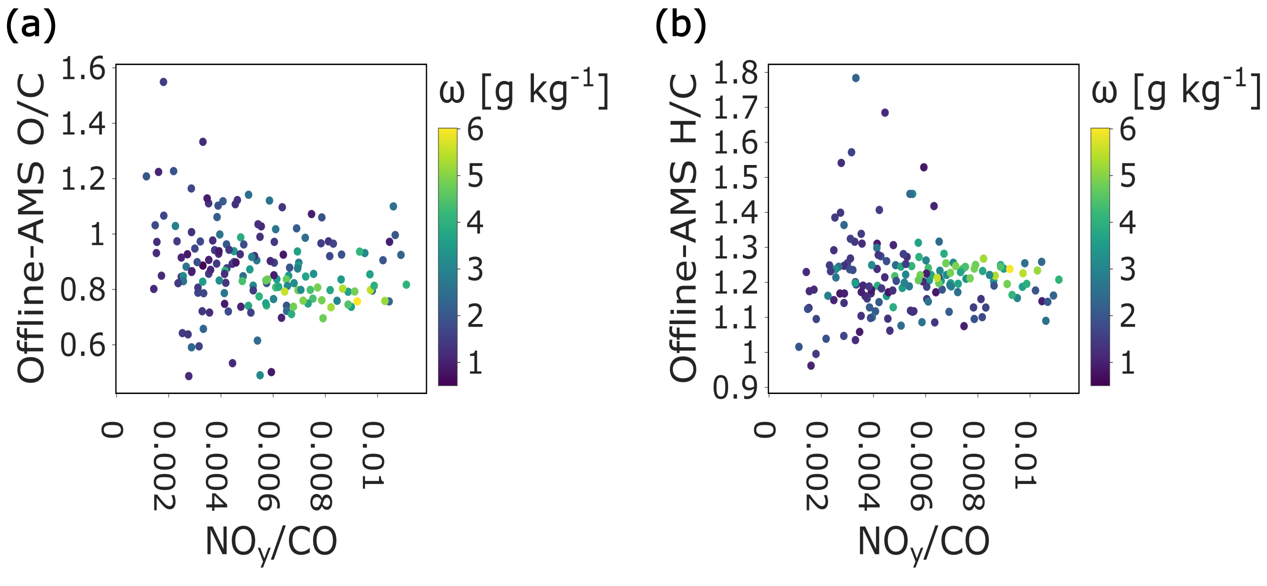

Figure S43. Offline-AMS atomic (a) O/C- and (b) H/C-ratios of the WSOA at JFJ as a function of the PBLi tracer NO_y/CO, colored by ω. Sampling dates dominated by Saharan dust were omitted from the plot.

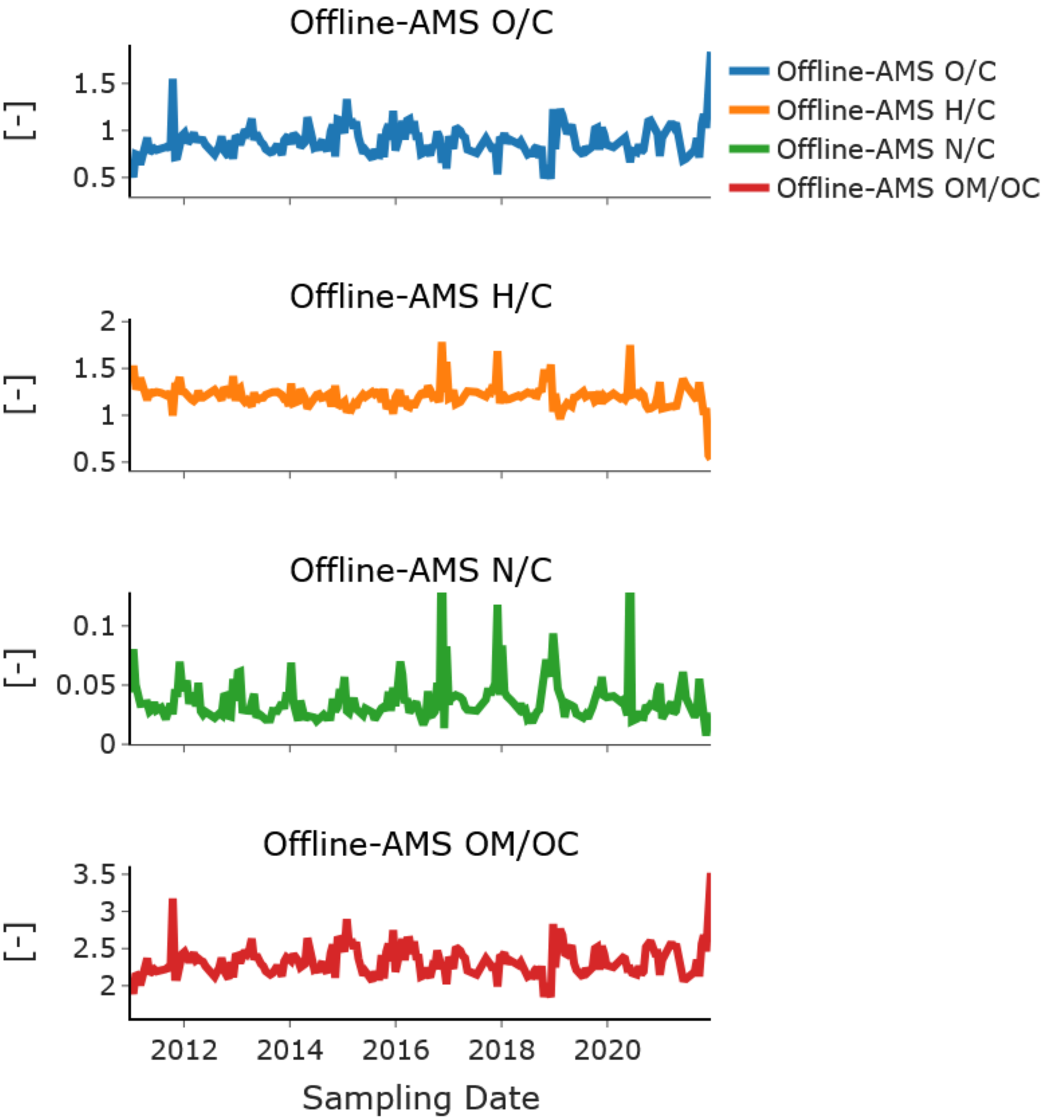

Figure S44. 11-year time series of Offline-AMS bulk atomic O/C-, H/C- and N/C-ratios as well as the OM/OC-ratio at the JFJ. Sampling dates dominated by Saharan dust were omitted from the plot.

S16 Overview of instruments and methods applied in this study

Table S2. Overview of the online meteorological and aerosol measurement instruments deployed at the JFJ, along with the corresponding derived analytical parameters utilized in this study. Periods of data coverage are specified, accompanied by additional remarks where necessary.

Analytical parameter	**Instrument**	**Data coverage**	**Comment**
Temperature, realtive humidity	Weather station with dew point mirror (Thygan, Meteolabor, Switzerland)	2011 to 2021	
Barometric pressure	Digital barometer PTB220 (Vaisala, Finland)	2011 to 2021	
Global solar radiation	Pyranometer CM21 (Kipp & Zonen B.V., Netherlands)	2011 to 2021	
Aerosol absorption coefficients	AE-31 (Magee Scientific, Slovenia), AE-33 (Magee Scientific, Slovenia)	2011 to 2021	used for Saharan dust detection; $\lambda =$ 370 nm, 470 nm, 520 nm, 590 nm, 660 nm, 880 nm, 950 nm; AE-31 data usage changed to AE-33 in 2015
Aerosol absorption coefficients, eBC	MAAP 5012, (Thermo Fisher Scientific, USA)	2011 to 2021	used for calculation of eBC; $\lambda =$ effectively 637 nm
Aerosol scattering coefficients	3563 (TSI, USA)	2011 to 2021	used for Saharan dust detection; $\lambda =$ 450 nm, 550 nm, 700 nm
Online PM_1 and PM_{10}	Fine dust monitor FIDAS 200 (PALAS, Germany)	October 2016 to 2021	Referenced to gravimetric PM_{10} standard method
gravimetric PM_{10}	HiVol filters collection and weighing before and after collection with high precision analytical balance XP205 (Mettler Toledo, USA)	2011 to 2021	filter conditioning at 20 °C and 50 % RH for 96 h

Table S3. Overview of the online gas-phase composition measurement instruments deployed at the JFJ, along with the corresponding derived analytical parameters utilized in this study. Periods of data coverage are specified, accompanied by additional remarks where necessary.

Analytical parameter	**Instrument**	**Data coverage**	**Comment**
CO	G2401 (Picarro, USA), APMA 360 and APMA 370 (Horiba, Japan)	2011 to 2021	AMPA changed to G2401 in 2012
NO	CLD 89p (Eco Physics, Switzerland)	2011 to 2021	
NO_2	CRANOX: PLC 762 (ANNOx, UK) + CLD 89p (Eco Physics, Switzerland)	2011 to 2021	
SO_2	43C TL and 43i TLE (Thermo Fisher Scientific, USA)	2011 to 2021	43C TL changed to 43i TLE in October 2011
O_3	49C and 49i photometric O_3 analyzer (Thermo Fisher Scientific, USA)	2011 to 2021	49C changed to 49i in July 2011
Non-methane hydrocarbons and halogenated VOCs	Medusa cold trap gas-chromatography mass spectrometry (Medusa GC-MS), custom-built pre-concentration unit and Agilent 5973 quadrupole mass spectrometer (Agilent Technologies, USA)	2011 to 2021	semi-continuous on-site at the JFJ

Table S4. Overview of the online PBLi tracer measurement instruments deployed at the JFJ, along with the corresponding derived analytical parameters utilized in this study. Periods of data coverage are specified, accompanied by additional remarks where necessary.

Analytical parameter	**Instrument**	**Data coverage**	**Comment**
N_{90}	Scanning mobility particle sizer (SMPS), custom build from differential mobility analyzer (DMA, TSI 3071, USA) and condensation particle counter (CPC, TSI 3775, USA)	2011 to 2021	according to specifications in Wiedensohler et al. (2012)
NO_y (sum of reactive N-species)	Converter + CLD 89p (Eco Physics, Switzerland)	2011 to 02/2020	conversion to NO on heated gold surface ($300\,^{\circ}\mathrm{C}$) (Zellweger et al., 2000)
^{222}Rn	two-filter dual flow loop design + $750\,\mathrm{L}$ ^{222}Rn detection chamber	2011 to 2012, 2016 to 2021	detection principle according to Griffiths et al. (2014)

Table S5. Overview of the offline HiVol filter based chemical parameters analyzed in this study, along with deployed instrumentation. Periods of data coverage are specified, accompanied by additional remarks where necessary.

Analytical parameter	**Instrument**	**Data coverage**	**Comment**
Bulk OC and EC concentration	OC-EC analyzer Model 5 (Sunset Lab, USA)	August 2013 to September 2014 and March 2019 to November 2019	OC converted to OA by Offline-AMS OM/OC-ratios
Bulk WSOC concentration	TOC-L-series (Shimadzu, Japan)	2011 to 2021 (4 day composites)	WSOC converted to WSOA by Offline-AMS OM/OC-ratios
Bulk WSOA concentration and composition, atomic- and OM/OC-ratios	Aerosol Mass Spectrometer, Long Time-of-Flight (Aerodyne, USA)	2011 to 2021 (4 day composites)	
Near-molecular organic composition	Extractive Electrospray Ionization Mass Spectrometer, Long Time-of-Flight (custom-designed inlet, MS from TOFWERK, Switzerland)	2011 to 2019 (4 day composites)	due to shifts in instrument sensitivity, the 2019 to 2021 EESI-MS data were only used for validation purposes
Major elements and trace metals	Inductively Coupled Plasma Mass Spectrometry (ICP-MS) iCAP TQ (Thermo Fisher Scientific, USA)	2011 to 2021 (4 day composites)	mild digestion of filters
Inorganic anions and cations, Molecular ID (di-)carboxylic acids	Ion Chromatography-Mass Spectrometry (IC-MS) with INTEGRION chromatography setup (Thermo Fisher Scientific, USA) and INTEGRION ISQ EC mass spectrometer (Thermo Fisher Scientific, USA)	2011 to 2021 (4 day composites)	
Molecular ID sugars and sugar alcohols	Ultra High Performance Liquid Chromatography-Tandem Mass Spectrometry (UHPLC-MS/MS) with ExionLC AD binary pump chromatography setup (Sciex, USA) and 5500 QTRAP tandem mass spectrometer (Sciex, USA)	2011 to 2021 (4 day composites)	

References

Aiken, A. C., DeCarlo, P. F., and Jimenez, J. L.: Elemental Analysis of Organic Species with Electron Ionization High-Resolution Mass Spectrometry, Analytical Chemistry, 79, 8350–8358, https://doi.org/10.1021/ac071150w, 2007.

Aiken, A. C., DeCarlo, P. F., Kroll, J. H., Worsnop, D. R., Huffman, J. A., Docherty, K. S., Ulbrich, I. M., Mohr, C., Kimmel, J. R., Sueper, D., Sun, Y., Zhang, Q., Trimborn, A., Northway, M., Ziemann, P. J., Canagaratna, M. R., Onasch, T. B., Alfarra, M. R., Prevot, A. S. H., Dommen, J., Duplissy, J., Metzger, A., Baltensperger, U., and Jimenez, J. L.: O/C and OM/OC Ratios of Primary, Secondary, and Ambient Organic Aerosols with High-Resolution Time-of-Flight Aerosol Mass Spectrometry, Environmental Science & Technology, 42, 4478–4485, https://doi.org/10.1021/es703009q, 2008.

Appenzeller, C., Begert, M., Zenklusen, E., and Scherrer, S. C.: Monitoring climate at Jungfraujoch in the high Swiss Alpine region, Science of The Total Environment, 391, 262–268, https://doi.org/10.1016/j.scitotenv.2007.10.005, 2008.

Baltensperger, U., Gäggeler, H. W., Jost, D. T., Lugauer, M., Schwikowski, M., Weingartner, E., and Seibert, P.: Aerosol climatology at the high-alpine site Jungfraujoch, Switzerland, Journal of Geophysical Research: Atmospheres, 102, 19 707–19 715, https://doi.org/10.1029/97JD00928, 1997.

Bros, P., Darfeuil, S., Jacob, V., Elazzouzi, R., Tusha, D., Rousseau, T., Weng, J., Winiger, P., El Haddad, I., Hueglin, C., Uzu, G., and Jaffrezo, J.-L.: Quantification of 21 sugars in tropospheric particulate matter by ultra-high-performance liquid chromatography tandem mass spectrometry, Atmospheric Measurement Techniques, 18, 6315–6327, https://doi.org/10.5194/amt-18-6315-2025, 2025.

Buck, A. L.: New Equations for Computing Vapor Pressure and Enhancement Factor, Journal of Applied Meteorology and Climatology, 20, 1527–1532, https://doi.org/10.1175/1520-0450(1981)020<1527:NEFCVP>2.0.CO;2, 1981.

Chow, J. C., Watson, J. G., Fujita, E. M., Lu, Z., Lawson, D. R., and Ashbaugh, L. L.: Temporal and spatial variations of PM2.5 and PM10 aerosol in the Southern California air quality study, Atmospheric Environment, 28, 2061–2080, https://doi.org/10.1016/1352-2310(94)90474-X, 1994.

Collaud Coen, M., Weingartner, E., Schaub, D., Hueglin, C., Corrigan, C., Henning, S., Schwikowski, M., and Baltensperger, U.: Saharan dust events at the Jungfraujoch: detection by wavelength dependence of the single scattering albedo and first climatology analysis, Atmospheric Chemistry and Physics, 4, 2465–2480, https://doi.org/10.5194/acp-4-2465-2004, 2004.

Cui, T., Manousakas, M. I., Wang, Q., Uzu, G., Hao, Y., Khare, P., Qi, L., Chen, Y., Han, Y., Slowik, J. G., Jaffrezo, J.-L., Cao, J., Prévôt, A. S. H., and Daellenbach, K. R.: Composition and Sources of Organic Aerosol in Two Megacities in Western China Using Complementary Mass Spectrometric and Statistical Techniques, ACS ES&T Air, 1, 1053–1065, https://doi.org/10.1021/acsestair.4c00051, 2024.

Daellenbach, K. R., Bozzetti, C., Křepelová, A., Canonaco, F., Wolf, R., Zotter, P., Fermo, P., Crippa, M., Slowik, J. G., Sosedova, Y., Zhang, Y., Huang, R.-J., Poulain, L., Szidat, S., Baltensperger, U., El Haddad, I., and Prévôt, A. S. H.: Characterization and source apportionment of organic aerosol using offline aerosol mass spectrometry, Atmospheric Measurement Techniques, 9, 23–39, https://doi.org/10.5194/amt-9-23-2016, 2016.

European Committee for Standardization (CEN): EN 12341:2023 – Ambient air — Standard gravimetric measurement method for the determination of the PM or PM. mass concentration of suspended particulate matter, 2023.

Fröhlich, R., Cubison, M. J., Slowik, J. G., Bukowiecki, N., Canonaco, F., Croteau, P. L., Gysel, M., Henne, S., Herrmann, E., Jayne, J. T., Steinbacher, M., Worsnop, D. R., Baltensperger, U., and Prévôt, A. S. H.: Fourteen months of on-line measurements of the non-refractory submicron aerosol at the Jungfraujoch (3580 m a.s.l.) – chemical composition, origins and organic aerosol sources, Atmospheric Chemistry and Physics, 15, 11 373–11 398, https://doi.org/10.5194/acp-15-11373-2015, 2015.

Griffiths, A. D., Conen, F., Weingartner, E., Zimmermann, L., Chambers, S. D., Williams, A. G., and Steinbacher, M.: Surface-to-mountaintop transport characterised by radon observations at the Jungfraujoch, Atmospheric Chemistry and Physics, 14, 12 763–12 779, https://doi.org/10.5194/acp-14-12763-2014, 2014.

Hao, Y., Strähl, J., Khare, P., Cui, T., Schneider-Beltran, K., Qi, L., Wang, D., Top, J., Surdu, M., Bhattu, D., Bhowmik, H. S., Vats, P., Rai, P., Kumar, V., Ganguly, D., Szidat, S., Uzu, G., Jaffrezo, J.-L., Elazzouzi, R., Rastogi, N., Slowik, J., Haddad, I. E., Tripathi, S. N., Prévôt, A. S. H., and Daellenbach, K. R.: Transported smoke from crop residue burning as the major source of organic aerosol and health risks in northern Indian cities during post-monsoon, Environment International, 202, 109 583, https://doi.org/10.1016/j.envint.2025.109583, 2025.

Herrmann, E., Weingartner, E., Henne, S., Vuilleumier, L., Bukowiecki, N., Steinbacher, M., Conen, F., Collaud Coen, M., Hammer, E., Jurányi, Z., Baltensperger, U., and Gysel, M.: Analysis of long-term aerosol size distribution data from Jungfraujoch with emphasis on free tropospheric conditions, cloud influence, and air mass transport, Journal of Geophysical Research: Atmospheres, 120, 9459–9480, https://doi.org/10.1002/2015JD023660, 2015.

Hueglin, C., Gehrig, R., Baltensperger, U., Gysel, M., Monn, C., and Vonmont, H.: Chemical characterisation of PM2.5, PM10 and coarse particles at urban, near-city and rural sites in Switzerland, Atmospheric Environment, 39, 637–651, https://doi.org/10.1016/j.atmosenv.2004.10.027, 2005.

Hueglin, C., Buchmann, B., Steinbacher, M., and Emmenegger, L.: The Swiss National Air Pollution Monitoring Network (NABEL) – Bridging Science and Environmental Policy, CHIMIA, 78, 722–727, https://doi.org/10.2533/chimia.2024.722, 2024.

Infante, H. G., Warren, J., Chalmers, J., Dent, G., Todoli, J. L., Collingwood, J., Telling, N., Resano, M., Limbeck, A., Schoenberger, T., Hibbert, D. B., LeGresley, A., Adams, K., and Craston, D.: Glossary of methods and terms used in analytical spectroscopy (IUPAC Recommendations 2019), Pure and Applied Chemistry, 93, 647–776, https://doi.org/10.1515/pac-2019-0203, 2021.

Jaffrezo, J.-L., Davidson, C. I., Kuhns, H. D., Bergin, M. H., Hillamo, R., Maenhaut, W., Kahl, J. W., and Harris, J. M.: Biomass burning signatures in the atmosphere of central Greenland, Journal of Geophysical Research: Atmospheres, 103, 31 067–31 078, https://doi.org/10.1029/98JD02241, 1998.

Jimenez, J. L., Jayne, J. T., Shi, Q., Kolb, C. E., Worsnop, D. R., Yourshaw, I., Seinfeld, J. H., Flagan, R. C., Zhang, X., Smith, K. A., Morris, J. W., and Davidovits, P.: Ambient aerosol sampling using the Aerodyne Aerosol Mass Spectrometer, Journal of Geophysical Research: Atmospheres, 108, https://doi.org/10.1029/2001JD001213, 2003.

Jin, X., Cai, X., Wang, X., Huang, Q., Song, Y., Kang, L., Zhang, H., and Zhu, T.: Water vapour exchange between the atmospheric boundary layer and free troposphere over eastern China: seasonal characteristics and the El Niño–Southern Oscillation anomaly, Atmospheric Chemistry and Physics, 24, 259–274, https://doi.org/10.5194/acp-24-259-2024, 2024.

Lopez-Hilfiker, F. D., Pospisilova, V., Huang, W., Kalberer, M., Mohr, C., Stefenelli, G., Thornton, J. A., Baltensperger, U., Prevot, A. S. H., and Slowik, J. G.: An extractive electrospray ionization time-of-flight mass spectrometer (EESI-TOF) for online measurement of atmospheric aerosol particles, Atmospheric Measurement Techniques, 12, 4867–4886, https://doi.org/10.5194/amt-12-4867-2019, 2019.

Miller, B. R., Weiss, R. F., Salameh, P. K., Tanhua, T., Greally, B. R., Mühle, J., and Simmonds, P. G.: Medusa: A Sample Preconcentration and GC/MS Detector System for in Situ Measurements of Atmospheric Trace Halocarbons, Hydrocarbons, and Sulfur Compounds, Analytical Chemistry, 80, 1536–1545, https://doi.org/10.1021/ac702084k, 2008.

Motos, G., Corbin, J. C., Schmale, J., Modini, R. L., Bertò, M., Kupiszewski, P., Baltensperger, U., and Gysel-Beer, M.: Black Carbon Aerosols in the Lower Free Troposphere are Heavily Coated in Summer but Largely Uncoated in Winter at Jungfraujoch in the Swiss Alps, Geophysical Research Letters, 47, e2020GL088 011, https://doi.org/10.1029/2020GL088011, 2020.

Müller, T., Henzing, J. S., de Leeuw, G., Wiedensohler, A., Alastuey, A., Angelov, H., Bizjak, M., Collaud Coen, M., Engström, J. E., Gruening, C., Hillamo, R., Hoffer, A., Imre, K., Ivanow, P., Jennings, G., Sun, J. Y., Kalivitis, N., Karlsson, H., Komppula, M., Laj, P., Li, S.-M., Lunder, C., Marinoni, A., Martins dos Santos, S., Moerman, M., Nowak, A., Ogren, J. A., Petzold, A., Pichon, J. M., Rodriquez, S., Sharma, S., Sheridan, P. J., Teinilä, K., Tuch, T., Viana, M., Virkkula, A., Weingartner, E., Wilhelm, R., and Wang, Y. Q.: Characterization and intercomparison of aerosol absorption photometers: result of two intercomparison workshops, Atmospheric Measurement Techniques, 4, 245–268, https://doi.org/10.5194/amt-4-245-2011, 2011.

Pandey Deolal, S., Brunner, D., Steinbacher, M., Weers, U., and Staehelin, J.: Long-term in situ measurements of NO$_x$ and NO$_y$ at Jungfraujoch 1998-2009: time series analysis and evaluation, Atmospheric Chemistry and Physics, 12, 2551–2566, https://doi.org/10.5194/acp-12-2551-2012, 2012.

Pieber, S. M., El Haddad, I., Slowik, J. G., Canagaratna, M. R., Jayne, J. T., Platt, S. M., Bozzetti, C., Daellenbach, K. R., Fröhlich, R., Vlachou, A., Klein, F., Dommen, J., Miljevic, B., Jiménez, J. L., Worsnop, D. R., Baltensperger, U., and Prévôt, A. S. H.: Inorganic Salt Interference on CO2+ in Aerodyne AMS and ACSM Organic Aerosol Composition Studies, Environmental Science & Technology, 50, 10 494–10 503, https://doi.org/10.1021/acs.est.6b01035, 2016.

Qi, L., Vogel, A. L., Esmaeilirad, S., Cao, L., Zheng, J., Jaffrezo, J.-L., Fermo, P., Kasper-Giebl, A., Daellenbach, K. R., Chen, M., Ge, X., Baltensperger, U., Prévôt, A. S. H., and Slowik, J. G.: A 1-year characterization of organic aerosol composition and sources using an extractive electrospray ionization time-of-flight mass spectrometer (EESI-TOF), Atmospheric Chemistry and Physics, 20, 7875–7893, https://doi.org/10.5194/acp-20-7875-2020, 2020.

Scheuvens, D., Schütz, L., Kandler, K., Ebert, M., and Weinbruch, S.: Bulk composition of northern African dust and its source sediments — A compilation, Earth-Science Reviews, 116, 170–194, https://doi.org/10.1016/j.earscirev.2012.08.005, 2013.

Venables, W. N. and Ripley, B. D.: Modern Applied Statistics with S, Statistics and Computing, Springer, New York, NY, ISBN 978-1-4419-3008-8 978-0-387-21706-2, https://doi.org/10.1007/978-0-387-21706-2, 2002.

Waked, A., Favez, O., Alleman, L. Y., Piot, C., Petit, J.-E., Delaunay, T., Verlinden, E., Golly, B., Besombes, J.-L., Jaffrezo, J.-L., and Leoz-Garziandia, E.: Source apportionment of PM$_{10}$ in a north-western Europe regional urban background site (Lens, France) using positive matrix factorization and including primary biogenic emissions, Atmospheric Chemistry and Physics, 14, 3325–3346, https://doi.org/10.5194/acp-14-3325-2014, 2014.

Wallace, J. M. and Hobbs, P. V.: Atmospheric science: an introductory survey, no. volume 92 in International geophysics series, Academic press, Amsterdam Paris, 2nd ed edn., ISBN 978-0-12-732951-2, 2006.

Whittlestone, S. and Zahorowski, W.: Baseline radon detectors for shipboard use: Development and deployment in the First Aerosol Characterization Experiment (ACE 1), Journal of Geophysical Research: Atmospheres, 103, 16 743–16 751, https://doi.org/10.1029/98JD00687, 1998.

Wiedensohler, A., Birmili, W., Nowak, A., Sonntag, A., Weinhold, K., Merkel, M., Wehner, B., Tuch, T., Pfeifer, S., Fiebig, M., Fjäraa, A. M., Asmi, E., Sellegri, K., Depuy, R., Venzac, H., Villani, P., Laj, P., Aalto, P., Ogren, J. A., Swietlicki, E., Williams, P., Roldin, P., Quincey, P., Hüglin, C., Fierz-Schmidhauser, R., Gysel, M., Weingartner, E., Riccobono, F., Santos, S., Grüning, C., Faloon, K., Beddows, D., Harrison, R., Monahan, C., Jennings, S. G., O'Dowd, C. D., Marinoni, A., Horn, H.-G., Keck, L., Jiang, J., Scheckman, J., McMurry, P. H., Deng, Z., Zhao, C. S., Moerman, M., Henzing, B., de Leeuw, G., Löschau, G., and Bastian, S.: Mobility particle size spectrometers: harmonization of technical standards and data structure to facilitate high quality long-term observations of atmospheric particle number size distributions, Atmospheric Measurement Techniques, 5, 657–685, https://doi.org/10.5194/amt-5-657-2012, 2012.

Zellweger, C., Ammann, M., Hofer, P., and Baltensperger, U.: NOy speciation with a combined wet effluent diffusion denuder – aerosol collector coupled to ion chromatography, Atmospheric Environment, 33, 1131–1140, https://doi.org/10.1016/S1352-2310(98)00295-7, 1999.

Zellweger, C., Ammann, M., Buchmann, B., Hofer, P., Lugauer, M., Rüttimann, R., Streit, N., Weingartner, E., and Baltensperger, U.: Summertime NOy speciation at the Jungfraujoch, 3580 m above sea level, Switzerland, Journal of Geophysical Research: Atmospheres, 105, 6655–6667, https://doi.org/10.1029/1999JD901126, 2000.

Zhang, Y., Favez, O., Canonaco, F., Liu, D., Močnik, G., Amodeo, T., Sciare, J., Prévôt, A. S. H., Gros, V., and Albinet, A.: Evidence of major secondary organic aerosol contribution to lensing effect black carbon absorption enhancement, npj Climate and Atmospheric Science, 1, 47, https://doi.org/10.1038/s41612-018-0056-2, 2018.